Geochemistry, Geophysics, Geosystems

RESEARCH ARTICLE
10.1029/2019GC008304

Authigenic Mineral Texture in Submarine 1979 Basalt Drill Core, Surtsey Volcano, Iceland

M. D. Jackson[1], S. Couper[1], C. V. Stan[2], M. Ivarsson[3,4], M. W. Czabaj[5], N. Tamura[6], D. Parkinson[6], L. M. Miyagi[1], and J. G. Moore[7]

[1]Department of Geology and Geophysics, University of Utah, Salt Lake City, UT, USA, [2]NIF and Photon Science, Livermore National Laboratory, Livermore, CA, USA, [3]Department of Biology and Nordic Center for Earth Evolution, University of Southern Denmark, Odense, Denmark, [4]Department of Palaeobiology, Swedish Museum of Natural History, Stockholm, Sweden, [5]Department of Mechanical Engineering, University of Utah, Salt Lake City, UT, USA, [6]Advanced Light Source, Lawrence Berkeley National Laboratory, Berkeley, CA, USA, [7]U.S. Geological Survey, Menlo Park, CA, USA

Key Points:
- Submarine basalt sampled 15 years after eruption records clay and zeolite mineral texture not previously observed in oceanic basalt
- Concentrically oriented crystallographic texture in nanocrystalline clay mineral and zeolite occurs in linear microstructures
- Carbonaceous matter of possible biological origin occurs in a linear microstructure and nanoscale cavities in altered olivine and glass

Supporting Information:
- Supporting Information S1

Correspondence to:
M. D. Jackson,
m.d.jackson@utah.edu

Citation:
Jackson, M. D., Couper, S., Stan, C. V., Ivarsson, M., Czabaj, M. W., Tamura, N., et al (2019). Authigenic mineral texture in submarine 1979 basalt drill core, Surtsey volcano, Iceland. *Geochemistry, Geophysics, Geosystems*, *20*, 3751–3773. https://doi.org/10.1029/2019GC008304

Received 1 MAR 2019
Accepted 1 JUN 2019
Accepted article online 22 JUN 2019
Published online 31 JUL 2019

Abstract Micrometer-scale maps of authigenic microstructures in submarine basaltic tuff from a 1979 Surtsey volcano, Iceland, drill core acquired 15 years after eruptions terminated describe the initial alteration of oceanic basalt in a low-temperature hydrothermal system. An integrative investigative approach uses synchrotron source X-ray microdiffraction, microfluoresence, micro-computed tomography, and scanning transmission electron microscopy coupled with Raman spectroscopy to create finely resolved spatial frameworks that record a continuum of alteration in glass and olivine. Microanalytical maps of vesicular and fractured lapilli in specimens from 157.1-, 137.9-, and 102.6-m depths and borehole temperatures of 83, 93.9, and 141.3 °C measured in 1980, respectively, describe the production of nanocrystalline clay mineral, zeolites, and Al-tobermorite in diverse microenvironments. Irregular alteration fronts at 157.1-m depth resemble microchannels associated with biological activity in older basalts. By contrast, linear microstructures with little resemblance to previously described alteration features have nanocrystalline clay mineral (nontronite) and zeolite (amicite) texture. The crystallographic preferred orientation rotates around an axis parallel to the linear feature. Raman spectra indicating degraded and poorly ordered carbonaceous matter of possible biological origin are associated with nanocrystalline clay mineral in a crystallographically oriented linear microstructure in altered olivine at 102.6 m and with subcircular nanoscale cavities in altered glass at 137.9-m depth. Although evidence for biotic processes is inconclusive, the integrated analyses describe the complex organization of previously unrecognized mineral texture in very young basalt. They provide a foundational mineralogical reference for longitudinal, time-lapse characterizations of palagonitized basalt in oceanic environments.

Plain Language Summary The thermal, chemical, and mineralogical evolution of basaltic rocks and the physical properties Earth's oceanic and continental crust are fundamentally linked. To better understand the evolution of basalt alteration over short geologic timescales, we turn to a newly formed volcanic island, Surtsey, in southern Iceland. The analyzed samples are composed of glassy basaltic fragments, created by explosive interactions between magma and seawater. They come from drill core collected in 1979, which was still hot when acquired 15 years after the eruptions ceased. The research focuses on (1) the alteration of the basaltic glass into secondary minerals and (2) tiny linear features formed of concentrically oriented secondary minerals. The partial dissolution of glass and its rapid transformation to clay mineral frees constituents that crystallize as zeolite and Al-tobermorite mineral cements. The linear features are composed of clay minerals (nontronite) and zeolite (amicite). Organic carbon-rich matter is associated with their clay mineral layers. These structures differ, however, from those in microtunnels ascribed to biologic activity in older basaltic rocks. The analyses provide a stepping stone toward understanding the earliest basaltic alteration in oceanic environments. Overall, our study demonstrates that basaltic and thereby crustal evolution is a more fast-paced, dynamic process than previously thought.

1. Introduction

The alteration of basaltic rock is a fundamental mineralogical process that has influenced the chemical and material properties of Earth's oceanic and continental crust for four billion years. Surtsey volcano, an isolated oceanic island created from 1963–1967 in the offshore extension of Iceland's southeast rift zone, provides an extremely well-constrained record of the initial stages of these alteration processes in a

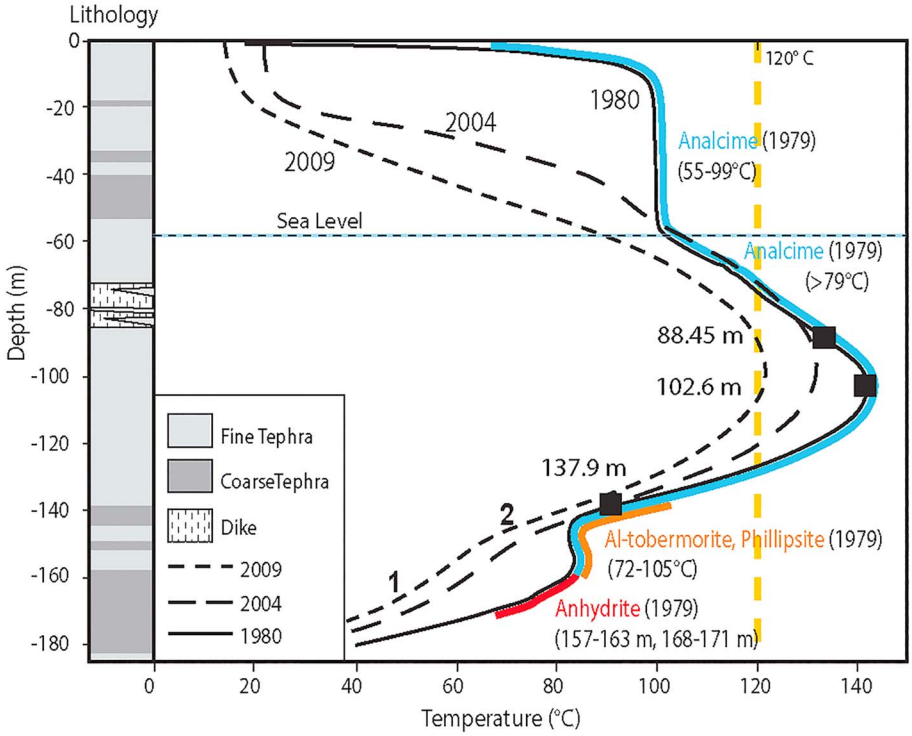

Figure 1. Temperature variation with depth in the 1979 Surtsey drill hole, 1980–2009. Lines along the 1980 curve show pronounced authigenic analcime (blue), Al-tobermorite and phillipsite (orange), and anhydrite (red) in the 1979 drill core (after *Jakobsson & Moore*, 1986; *Jackson* et al., 2015). Mineral assemblages are the cumulative result of fluid-rock interactions prior to 1979, while temperatures are relevant to the year of the measurement. Microbiological analyses of downhole water sampling revealed diverse subterrestrial bacterial and archaeal sequences at 172 m (54 °C in 2009; site 1) and 145 m (80 °C in 2009; site 2; *Marteinsson* et al., 2015). The 120 °C line represents the inferred temperature maximum for functional microbial life (*Ivarsson* et al., 2009; *Kashefi & Lovley*, 2003; *Prieur & Marteinsson*, 1998).

hydrothermal system that traverses submarine and subaerial basaltic tephra, tuff, and minor intrusions (Thórarinsson, 1967; Jakobsson, 1978; Jakobsson & Moore, 1982, 1986; Figure 1). Explosive eruptions from 1963–1964 constructed the island from a seafloor depth of 130 m below sea level; mainly effusive eruptions followed from 1964–1967 (Jakobsson et al., 2009; Thórarinsson, 1967). The basalt contains plagioclase, olivine, and Cr-spinel phenocrysts (Jakobsson & Moore, 1986). Progressive geochemical changes over 3.5 years of eruption suggest magmatic mixing of depleted ridge basalt with ponded, enriched alkali basalt at the propagating ridge axis (Schipper et al., 2015). A 181-m-deep, vertical, cored hole that was drilled in 1979 transected vesicular, glassy basalt tuff above sea level and deeply palagonitized tuff with zeolite and Al-tobermorite mineral cements below sea level (Jakobsson & Moore, 1982, 1986). A hydrothermal anomaly, in which a maximum borehole fluid temperature, 141.3 °C measured in 1980, occurred at 100- to 106-m depth below surface (Figure 1), is thought to be a convective system that developed in response to basaltic intrusions that fed lava flows from 1964–1967 (Jakobsson, 1978; Jakobsson & Moore, 1982; Stéfansson et al., 1985). Subterrestrial bacterial and archaeal sequences have been identified in borehole fluids below the temperature maximum (Marteinsson et al., 2015). The International Continental Scientific Drilling Program SUSTAIN project (Jackson et al., 2015) drilled three new cored boreholes through the still hot volcano in 2017 (Jackson et al., 2019).

Investigations of the 1979 Surtsey drill core in the early 1980s revealed that rates of alteration, recorded by the thickness of an alteration rim around olivine crystal fragments and ash- and lapilli-sized particles of sideromelane that strongly increased with temperature (Jakobsson & Moore, 1986). Nontronite, an iron-rich, smectitic clay mineral, occupied these alteration rims. The dissolution of glass produced alkaline solutions from which authigenic minerals crystallized. These are principally analcime, phillipsite, and anhydrite (Figure 1). Analcime is a cubic, sodic zeolite ($Na(AlSi_2O_6)\cdot H_2O$); phillipsite is a monoclinic, calcic, sodic, and potassic zeolite ($((Ca,Na_2,K_2)_3Al_6Si_{10}O_{32}\cdot 12H_2O$); and anhydrite is an orthorhombic calcium sulfate

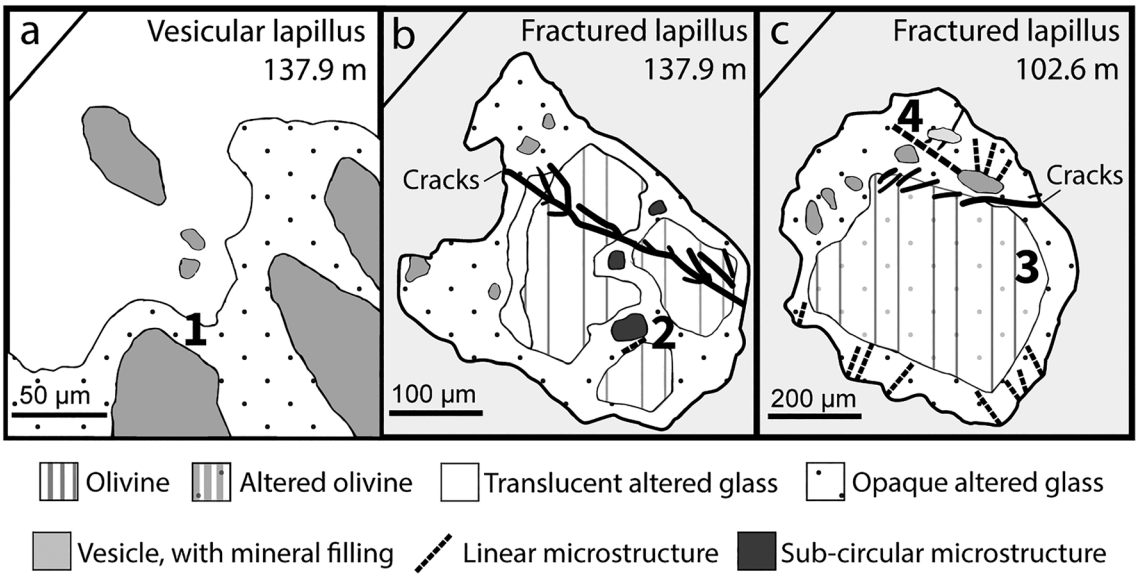

Figure 2. Examples of integrated analytical investigations in the lapilli of submarine 1979 Surtsey drill core samples. (a) Vesicular lapillus, 137.9-m depth, 93.9 °C in 1980, **1**, altered glass rim: X-ray microdiffraction (μXRD), scanning transmission electron microscopy, Raman spectroscopy (Figures 5 and 6). (b) Fractured lapillus with olivine, 137.9 m, **2**, subcircular and linear microstructures: X-ray microfluorescence (μXRF) and μXRD (Figures 8 and 9). (c) Fractured lapillus with olivine, 102.6 m, 141.3 °C in 1980, **3**, altered olivine: μXRF, μXRD, scanning transmission electron microscopy, and Raman spectroscopy; **4**, linear microstructure μXRF and μXRD (Figures 10–13).

($CaSO_4$). Al-tobermorite, an unusual calcium-silicate-hydrate phyllosilicate with 11.3- to 11.4-Å (002) *d* spacing (Jackson et al., 2013), occurs throughout and is especially well developed in the submarine hydrothermal system. Crystallization sequences record phillipsite growing from clay mineral (5.6 m, 70 °C in 1980), Al-tobermorite growing from dissolving phillipsite laths (37 m, 100 °C, in 1980), and analcime growing with clay mineral and Al-tobermorite (82.7 m, 135 °C, in 1980; Jakobsson & Moore, 1986, Figure 8). These relationships indicate wide-ranging solution-rock interactions that produced diverse mineral assemblages and rapid rates of alteration in fine-scale microenvironments under a broad range of hydrothermal fluid and temperature conditions.

The central purpose of this article is to describe the mineralogical results of hydrothermal seawater fluid interactions with very young basaltic tephra and the physical relationships among the materials formed by the alteration of basaltic glass, or sideromelane, and olivine. Micrometer- to nanometer-scale palagonitic alteration features are described in submarine samples at 150.1-, 137.9-, and 102.6-m depths in the 1979 Surtsey drill core using chemical, mineralogical, and spectroscopic analytical techniques not available in the 1980s to build on previous investigations (Jakobsson & Moore, 1982, 1986; Figure 1). The research objectives aim to inform a fundamental question: What processes control the conversion of young oceanic basaltic glass and olivine into authigenic mineral assemblages?

The first objective is to demonstrate how multiple integrated microanalytical methods can provide finely resolved, spatial frameworks for understanding the structural organization of authigenic mineral growth and the associated elemental concentrations of relevant cations in diverse microenvironments. We simultaneously integrate maps of instructive microstructures using synchrotron source X-ray microdiffraction (μXRD), X-ray microfluorescence (μXRF), micro-computed tomography (μCT), and scanning transmission electron microscopy (S/TEM) coupled with Raman spectroscopy. Figure 2 provides examples of the sites of the overlapping analytical investigations in a vesicular lapillus and in fractured lapilli containing olivine crystal fragments. Figure 3 provides a mineralogical context for the microanalytical investigations in terms of palagonitic alteration processes. Subsequent micrometer-scale maps illustrate the spatial and sequential maturation of nanocrystalline clay mineral in the altered glass of vesicular lapilli (Figures 4–6) and in fractured lapilli containing olivine crystals (Figures 6–13 and Figures S1–S5 in the supporting information). The second objective is to provide fresh perspectives for understanding how spatial distributions of authigenic mineral assemblages record a continuum of alteration at the micrometer scale. The associated elemental

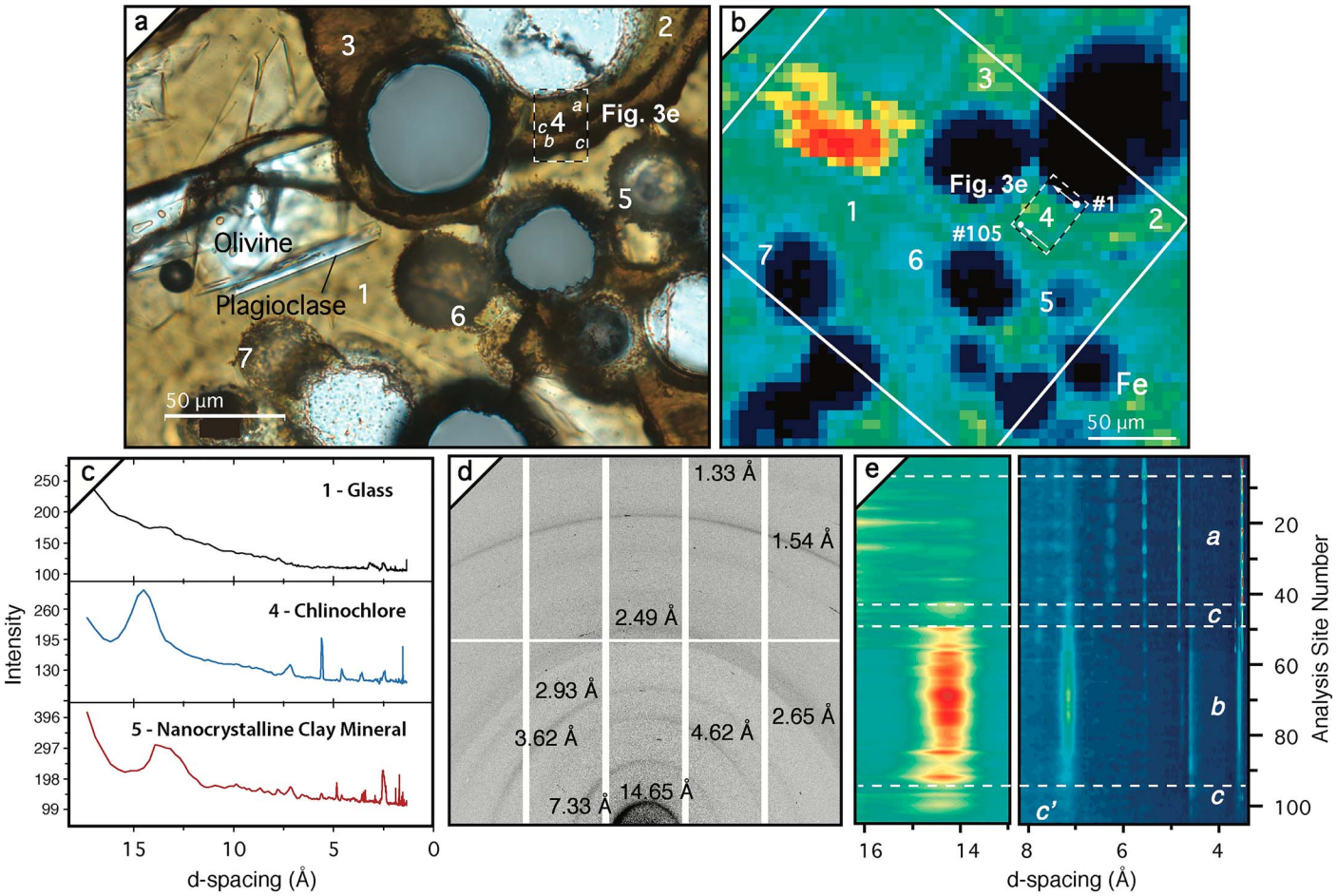

Figure 3. Basaltic lapillus, 157.1-m depth, showing fresh glass and rinds of altered glass around vesicles (see also Figure S1). (a) Petrographic image, plane polarized light, and sites of analyses 1–7. In site 4, X-ray microdiffraction (μXRD) results for zones *a*, *b*, *c*, and *c′* are shown in (e). (b) X-ray microfluorescence map, Fe, relative concentration increases from blue to yellow to red. (c) Intensity versus *d* spacing for μXRD analyses at sites 1, 4, and 5 and integration of 10–63° 2θ (1.47- to 17.76-Å *d* spacing) over ±35°χ. (d) μXRD diffraction image for site 4. (e) μXRD map of site 4. Reading down the *y* axis gives the sequential acquisition of analyses, 1–105, where each row shows the relative intensity counts for each *d* spacing on the *x* axis, from 3.5–8 and 13–16 Å. The locations of zones *a*, *b*, *c*, and *c′* are shown in (a). Intensity increases from blue to yellow to red.

concentrations of relevant cations, such as calcium, iron, and titanium, and the crystallographic characteristics of nanocrystalline clay mineral are described. The third objective is to investigate linear microstructures with clay and zeolite mineral textures in the altered glass and olivine of fractured lapilli, whose morphological features only vaguely resemble putative biological features in other igneous rocks (Fisk et al., 2003; Fisk & McLoughlin, 2013; Furnes et al., 2001; Nikitczuk et al., 2016; Thorseth et al., 1991, 1992, 2001; Türke et al., 2018; Walton, 2008).

The techniques demonstrated here provide an introductory analytical foundation for reexamining the initiation of palagonitic alteration processes, which may not be preserved in older basaltic deposits. They situate the continuum of alteration that produces palagonitic mineral assemblages in oceanic basalt within a young, very well-constrained volcanic system. This could eventually serve as a natural analog that quantifies the roles of glass and solution composition, temperature, rates of solution renewal, and the behavior of crystals to predict the stability of nuclear waste borosilicate glasses (Jantzen et al., 2010, 2017; Parruzot et al., 2015). The analytical results form a foundation for future investigations of the alteration of Surtsey tephra and a valuable reference for comparisons with the 2017 drill cores acquired by the International Continental Scientific Drilling Program SUSTAIN project (Jackson et al., 2015, 2019). The investigations further inform the record of alteration rates and processes in seafloor basalts, which ultimately scale up to influence geochemical pathways and the evolving mineralogical and physical properties of the oceanic crust.

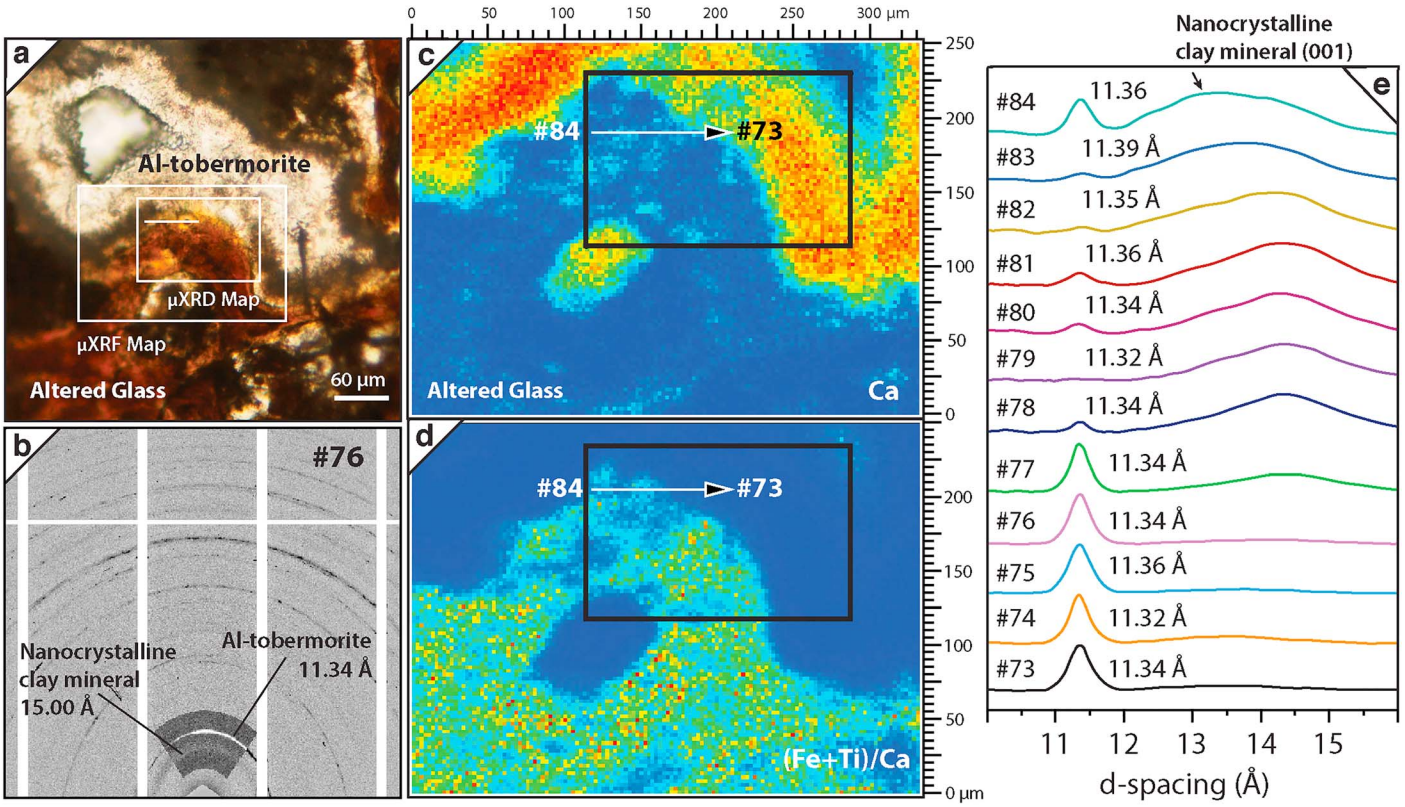

Figure 4. Basaltic lapillus, 137.9-m depth, showing altered glass, crystallization of Al-tobermorite in a vesicle partially filled with accretionary fine ash, and maturation of nanocrystalline clay mineral. (a) Petrographic image, plane polarized light. (b) X-ray microdiffraction (μXRD) diffraction image for analysis #76 and integration of 3.5–7.9° 2θ (20- to 9-Å *d* spacing) over ±35°χ. See (e) for the *d* spacing intensity plot. (c, d) X-ray microfluorescence (μXRF) maps, Ca, and (Fe +Ti)/Ca. (e) Intensity versus *d* spacing plot for nanocrystalline clay mineral and Al-tobermorite mapped at 5-μm increments along a 180-μm traverse with the integration described in (b).

2. Palagonitization Processes

Palagonitization is an ill-defined process that modifies the properties of basaltic volcanic glass through chemical interactions with water and the activity of microorganisms (Fisk et al., 2003; Furnes et al., 2001; Pauly et al., 2011; Stroncik & Schmincke, 2001). It contributes to a continuum of alteration in basaltic tephra, tuffs, and lavas. The alteration of fresh basaltic glass to an optically clear, isotropic material, or "gel-palagonite" and then to an optically anisotropic, birefringent material, or "fibro-palagonite" (Peacock, 1926) involves continuous chemical transitions (Furnes, 1978; Furnes et al., 2001; Hay & Iijima, 1968; Staudigel & Hart, 1983; Stroncik & Schmincke, 2001, 2002; Walton & Schiffman, 2003). Progressive selective or congruent dissolution, hydrolysis, hydration, and oxidation of basaltic glass in marine and meteoric water systems produces authigenic mineral assemblages of smectitic clay mineral, zeolites, phyllosilicates, and Fe oxyhydroxides (e.g. Crovisier et al., 2003; Hay & Iijima, 1968; Jakobsson & Moore, 1986; Moore, 1966; Pauly et al., 2011; Staudigel & Hart, 1983; Stroncik & Schmincke, 2002; Thorseth et al., 1991, 2003). The sharp contact with fresh glass that separates the altered glass rind (and the parallel alteration layers that form in some specimens) may represent the solution interface at prior stages of alteration (e.g., Hay & Iijima, 1968, Figure 6; Stroncik & Schmincke, 2001, Figure 3; Pauly et al., 2011, Figure 14). "Palagonite," the clear, transparent, thermodynamically unstable, gel-like, amorphous alteration product of basaltic glass, has been suggested as a preferred term for gel-palagonite (Stroncik & Schmincke, 2001).

The early stages of glass aging and maturation are thought to form a two-phase system, consisting of palagonite and crystalline material, principally clay mineral (Staudigel & Hart, 1983; Stroncik & Schmincke, 2001). The transition to fibro-palagonite involves further crystallization of the clay mineral and additional chemical and mineralogical changes. Geochemical studies of palagonitized basalts show a great deal of variation and indicate that multiple factors influence glass alteration mechanisms and rates, even at the

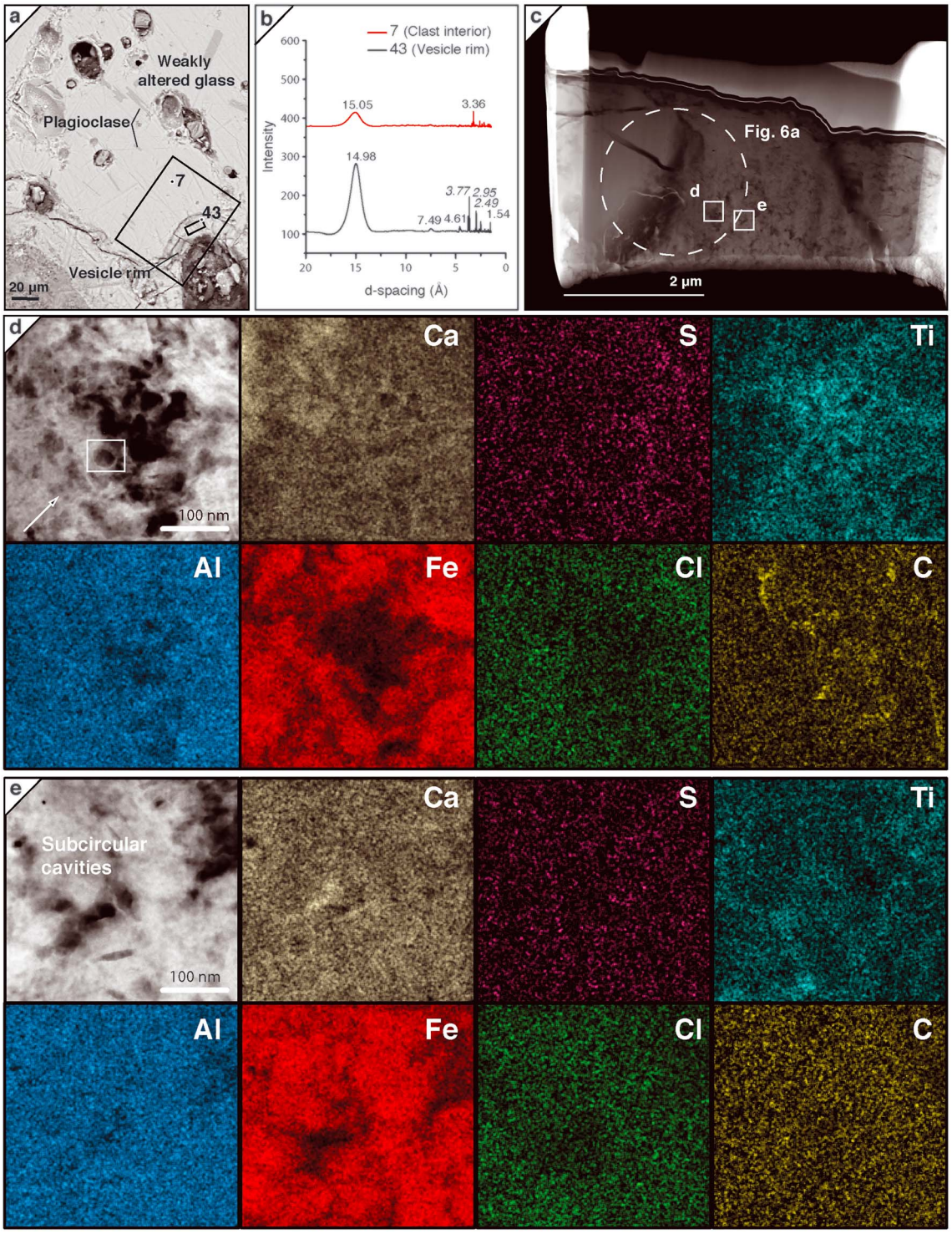

Figure 5. Basaltic lapillus, 137.9-m depth, showing investigations of altered glass. (a) Scanning electron microscopy-backscattered electron image, sites of X-ray microdiffraction(μXRD) analyses and focused ion beam (FIB) lift out. (b) Intensity versus *d* spacing plot for μXRD analyses (#7 [red] and #43 [black], including plagioclase [shown in italics]). (c) FIB lift out, site of Raman spectra (Figure 7a). (d) Scanning transmission electron microscopy-energy dispersive X-ray spectrometer (S/TEM EDS) elemental maps, white rectangle indicates a subcircular cavity along the left edge of the vesicle and very fine nanoscale cavities nearby (arrow). (e) S/TEM EDS elemental maps, area of larger nanoscale subcircular cavities.

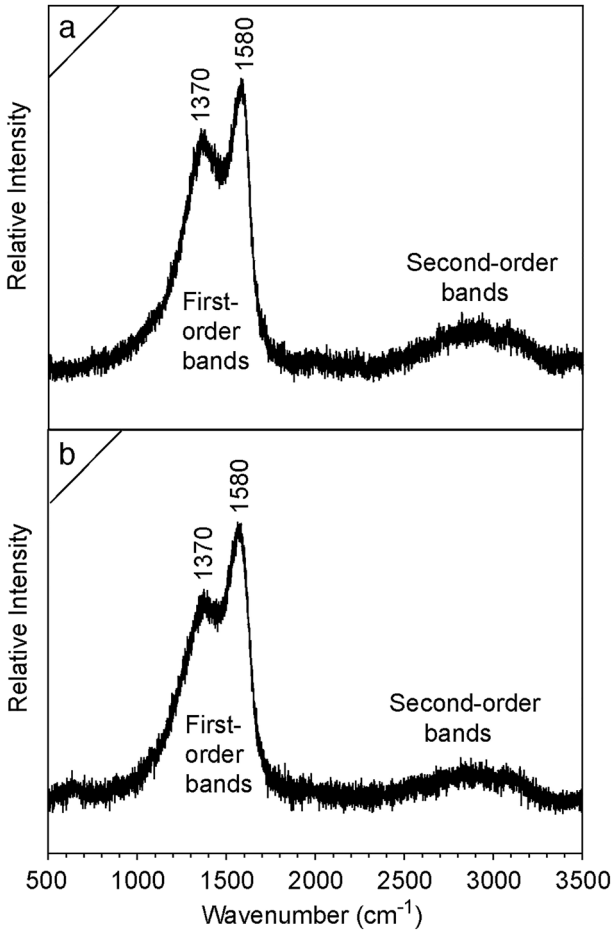

Figure 6. Raman spectra of authigenic nanocrystalline clay mineral microstructures in focused ion beam lift outs. (a) Altered glass rind along a vesicle perimeter, basaltic lapillus, 137.9-m depth (Figure 5). (b) Concentrically oriented microstructure in an olivine crystal, 102.6-m depth (Figures 10–12).

intergrain scale: time, temperature, reactive surface area, structure and growth rates of authigenic phases, and fluid properties and flow rates that are influenced by changing porosity, permeability, and pressure gradients (e.g. Pauly et al., 2011; Staudigel & Hart, 1983; Stroncik & Schmincke, 2001, 2002). Many studies have measured variations in the chemical composition of palagonitized glass, yet little is known about the fine-scale crystallographic differentiation, distribution, and texture of authigenic minerals in this material.

Recent experimental studies and geochemical modeling of basaltic glass alteration situate laboratory mechanisms and rates in the context of transition state theory and stages of glass corrosion. They quantify the roles of initial glass and solution composition, temperature, rates of solution renewal, and the behavior of crystals within basaltic glass to predict glass stability, especially for high-level nuclear waste borosilicate glass (Crovisier et al., 2003; Gislason & Oelkers, 2003; Jantzen et al., 2010, 2017; Oelkers & Gislason, 2001; Parruzot et al., 2015). These studies inform those of natural analogs such as the Surtsey system, which encompasses a broad range of well-constrained environmental conditions.

Fine-scale biotic alteration features occur in basalts worldwide, from Holocene subglacial eruptions to Precambrian ophiolites and greenstones, mainly as granular and tubular textures that dissolve volcanic glass (Furnes et al., 2001; Staudigel et al., 2008, 2015; Thorseth et al., 1991, 2001, 2001, 2003). Fossilized endolithic fungal structures also occur in igneous oceanic crust, dating to 2.4 Ga (Bengtson et al., 2017). Many studies describe the morphological features of glass dissolution cavities and their complex expression as microchannels or microtubules, which commonly form narrow protrusions along fractures and at the interface between fresh and altered basaltic glass (Figures 3 and S1). These microstructures are thought to record microbial microboring into glass (e.g., McLoughlin et al., 2010, Figure 1; Fisk et al., 2003, Figure 2; Staudigel et al., 2008, Figure 15; Walton, 2008, Figure 1). Studies of alteration in 1- to 122-Ma oceanic basalts focus mainly on morphological, chemical, and isotopic investigations (Alt & Mata, 2000; Benzerara et al., 2007; Furnes et al., 2001; Kruber et al., 2008; Thorseth et al., 1991, 1992; Torsvik et al., 1998). Microstructural studies of oceanic basalt drill cores, for example, describe subcircular alteration features that preserve geochemical signatures associated with concentrically layered packets of phyllosilicate minerals surrounded by a narrow rim of altered glass (Alt & Mata, 2000; Fliegel et al., 2012; Knowles et al., 2012). Little is known, however, about how abiotic and biotic alteration products might organize themselves into authigenic mineral texture with crystallographic preferred orientation.

3. Sample Selection and Analytical Methods

3.1. Sample Selection

Three submarine tuff samples from the 1979 Surtsey drill core archive were stored in wooden core boxes at room temperature (~18 °C) at the Iceland Institute for Natural History. They were selected on the basis of mineralogical, geochemical, and microscopic descriptions of the 1979 core (Jakobsson & Moore, 1986) and the diverse processes of alteration recorded in their glass and olivine components observed during comprehensive petrographic investigations of a suite of 11 newly fabricated thin sections from the 1979 drill core archive. The samples comprise a weakly coherent olive gray (5Y 5/1) tuff at 157.1-m depth, a well-consolidated olive black (5Y 2/1) tuff at 137.9 m, and a compact, well-cemented olive-gray (5Y 3/1) tuff at 102.6-m depth (Figure 1). All Munsell color notation is referenced to the Geological Society of America Rock Color Chart. The sampling sites correspond to moderate temperatures near the base of the borehole (157.1 m, 83 °C in 1980), slightly elevated temperatures in the zone of greatest Al-

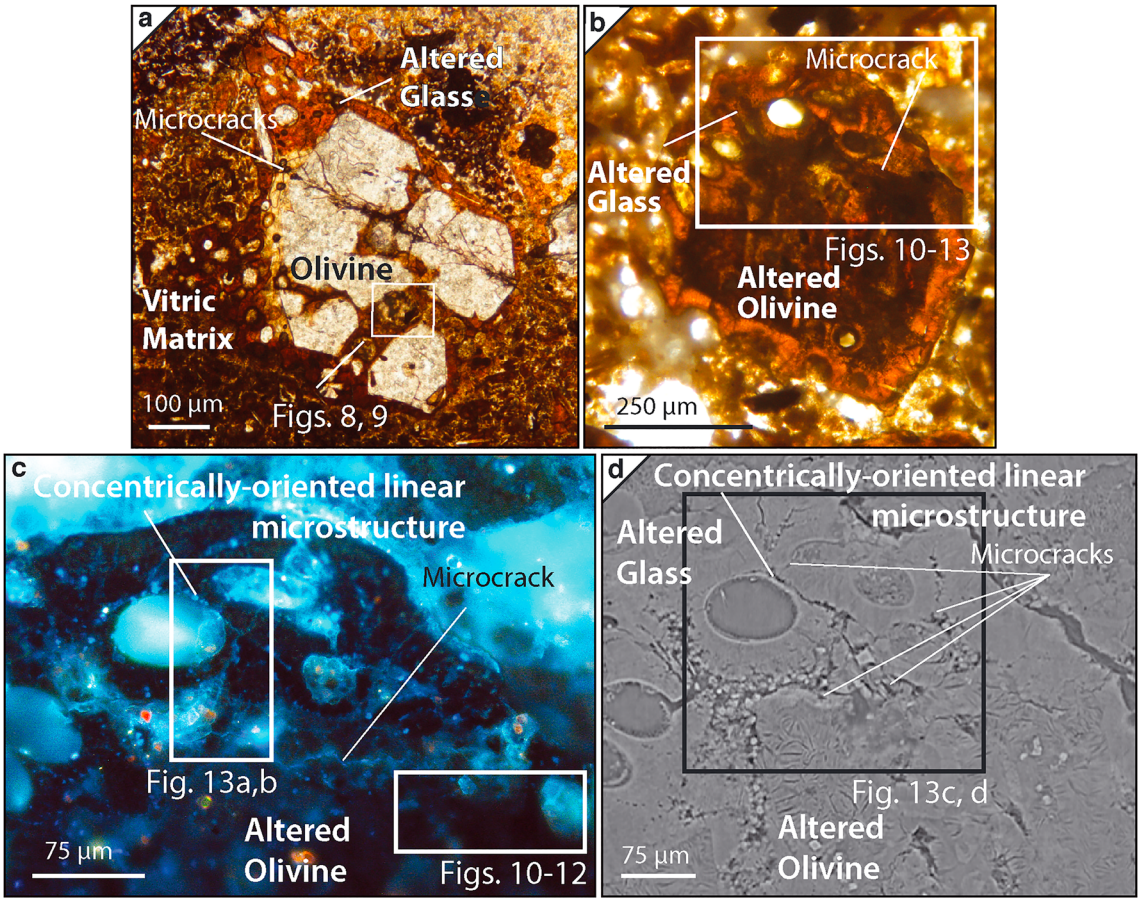

Figure 7. Fractured lapilli, with olivine crystals enrobed in altered basaltic glass. (a) Mainly intact olivine, 137.9-m depth, and subcircular microstructures in altered glass, petrographic image (Figures 8 and 9). (b) Strongly altered olivine, 102.6-m depth, with a 75- to 100-µm altered glass rim, petrographic image (Figures 10–13). (c) Ultraviolet-excited native fluorescence image of a detail of (b). Note that larger fluorescent areas are superglue adhesive. (d) X-ray tomograph of (c), showing the area of micro-computed tomography analysis (Figure 13).

tobermorite production (137.9 m, 93.9 °C in 1980), and the maximal temperature of the hydrothermal system (102.6 m, 141.3 °C in 1980). Differences in alteration with depth follow observations by Jakobsson and Moore (1986) and indicate that authigenic processes occurred syngenetically in the hydrothermal submarine environment.

3.2. Analytical Methods

3.2.1. Petrographic Microscopy

Studies of polished thin sections used plane polarized light, reflected light, and ultraviolet (UV) light with an Olympus BX53M microscope with U-RFL-T and U-RX-T mercury and xenon burners in the Bowen Laboratory, Department of Geology and Geophysics, University of Utah, to identify instructive sites for the micrometer-scale maps. The UV-excited, untreated epifluorescence microscopy on polished thin sections used wideband UV 365-nm illumination at 60-s exposure, as a qualitative indicator of native fluorescence and possible detection and localization of organic signatures (Bhartia et al., 2010; Salas et al., 2015). The term “texture” specifies crystallographic preferred orientation rather than rock fabric components (Wenk & Van Houtte, 2004).

Superglue™ adhesive was used in the preparation of the polished thin sections, and the areas selected for microanalyses were cut from the glass-mounted thin section with a saw. The 0.3-mm thick rock slices were detached from the glass with nitromethane and mounted on adhesive tape for successive investigations of the same microstructure with diffraction and spectroscopic methods.

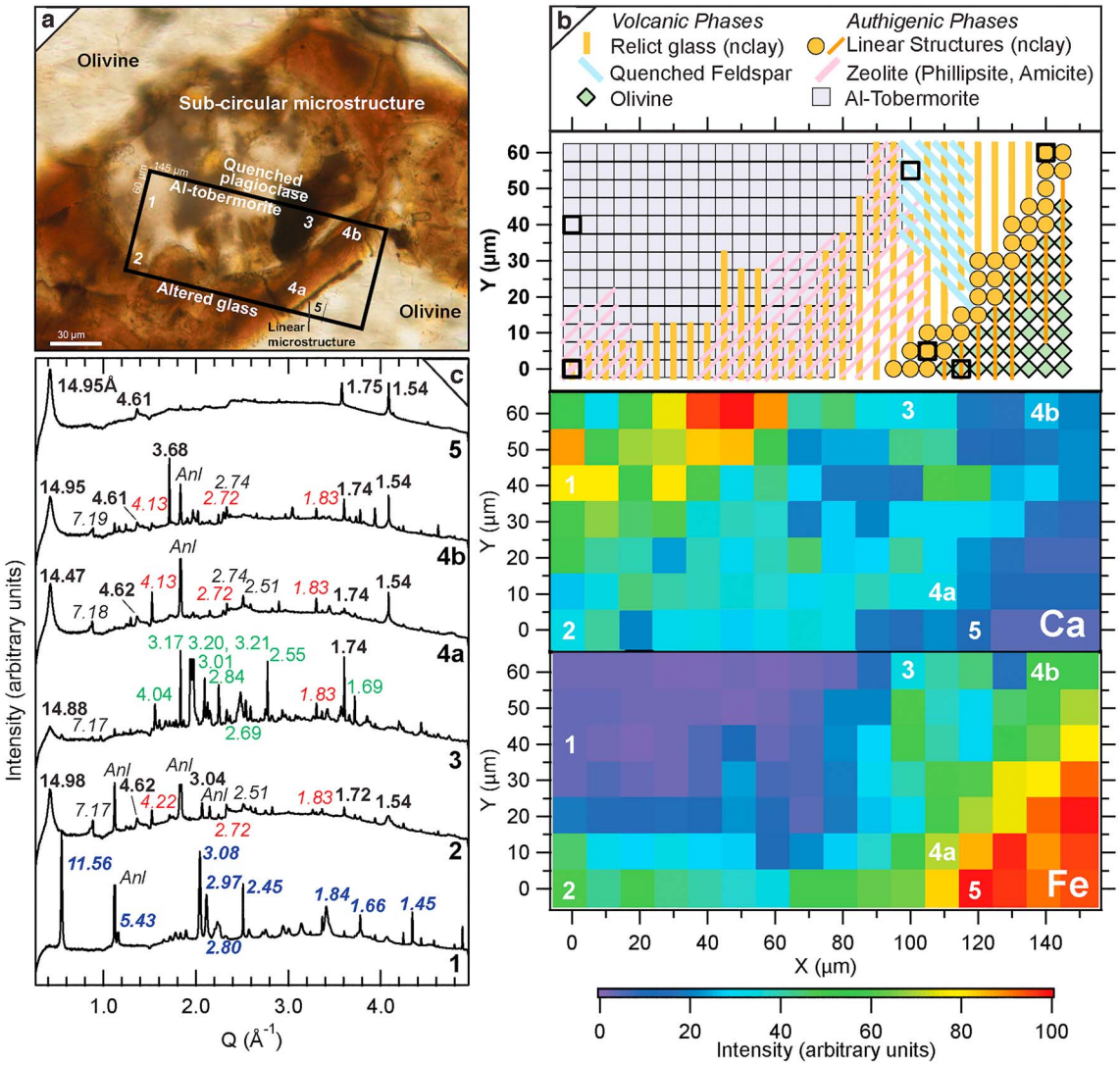

Figure 8. Fractured lapillus, 137.9-m depth, with olivine crystals and a subcircular microstructure in altered glass (Figures 7a, 9, and S2–4). (a) Petrographic image, authigenic mineral zones (1) Al-tobermorite, (2) altered glass, (3) quenched plagioclase, (4) linear nanocrystalline clay mineral microstructures, and (5) olivine single crystal. Note the fine dark linear features at the upper left corner of the olivine crystal (4b). (b) Mineral phases are mapped with X-ray microdiffraction (µXRD) analyses in a 60 × 145-µm^2 grid at 5-µm step size and qualitative X-ray microfluorescence (Ca and Fe) analyses are shown at 10-µm step size. (c) Intensity versus Q (Å^{-1}) plot for µXRD analyses, in zones 1–5: 1, #5; 2, #13; 3, #262; 4a, #285; 4b, #365; and 5, #312 (Figure S4). Plagioclase (labradorite; green), nontronite (bold, black), Al-tobermorite (bold italic, blue), phillipsite (italic, black), amicite (italic, red), and analcime (Anl).

3.2.2. Scanning Electron Microscopy

Scanning electron microscopy-backscattered electron images were obtained with the Zeiss EVOMA10 scanning electron microscope at the Department of Earth and Planetary Science at University of California, Berkeley. The imaging was performed at a beam energy of 15 keV and beam current of 850 pA.

3.2.3. Synchrotron µXRD and µXRF

Experiments at Advanced Light Source Beamline 12.3.2 investigated submicron-sized crystals with powder microdiffraction using a monochromatic beam and olivine single crystals with Laue microdiffraction using a polychromatic beam (Stan & Tamura, 2018; Tamura et al., 2009). The rock slice mounted on tape was loaded in transmission mode, with the detector placed at 39° to the incident beam. A monochromatic X-ray beam of 8 or 10 keV was focused to 2 × 5-µm spot size. A DECTRIS Pilatus 1M area detector placed at about 150-mm recorded Debye rings from crystalline phases. The experimental geometry was calibrated using α-Al_2O_3 powder. X-ray diffractograms were produced with *d* spacing reflections integrated radially for 2θ 3–54° mainly over a 76° arch segment (χ) around the cone of diffraction. These are shown as intensity

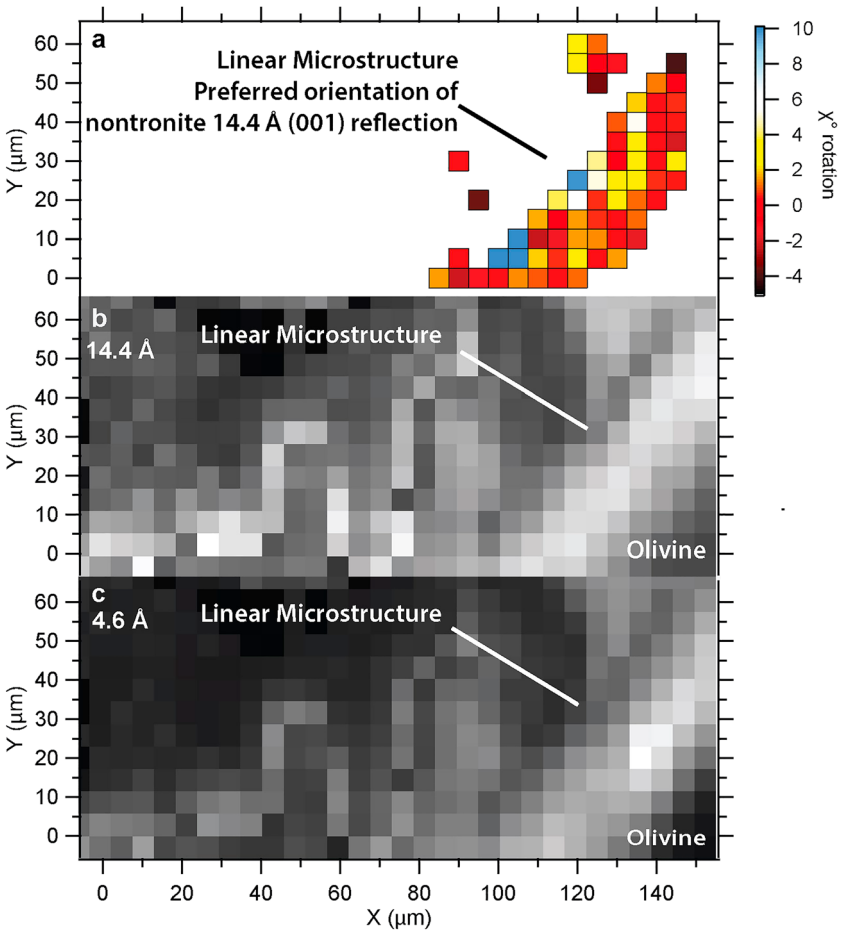

Figure 9. Nanocrystalline clay mineral (nontronite) *d* spacings acquired at 5-µm step size in the mapped area of Figure 8. (a) The 4.6-Å (020) reflection rotates through an arch segment of 8° to −4°χ along the long linear microstructure. (b, c) A grayscale grid shows the distribution and intensity of nontronite 14.4-Å (001) and 4.6-Å *d* spacings. Intensity increases from black to gray to white.

versus *d* spacing plots to illustrate variations in nanocrystalline clay mineral reflections or as intensity versus $Q = 2\pi/d$ spacing to increase the readability of lower *d* spacing reflections from other phases. Point-to-point µXRD scans with 3-, 5-, or 10-µm step size reveal the distribution of minerals and their *d* spacings and crystallographic preferred orientations, referenced to qualitative calcium (Ca), iron (Fe), or titanium (Ti) µXRF scans. Numbered points (e.g., Figure 4, #76) correspond to a specific analysis that can be referenced spatially in the map grid or data set. Nanocrystalline patterns are obtained from crystallites <<2 µm in size, which produce broad, diffuse bands in the cone of diffraction generated by the monochromatic X-ray beam. Single-crystal Laue microdiffraction scans were collected on select olivine crystals using a 10-µm step size, and modeled as forsterite. All data were processed using the XMAS software (Tamura, 2014).

3.2.4. S/TEM

Focused ion beam (FIB) milling with the Helios Nanofab 650 Dual Beam Microscope at the University of Utah Surface Analysis Laboratory produced two thin film lift outs from microstructures previously studied with synchrotron source µXRF and µXRD experiments. Ion beam-deposited platinum, a platinum carbon compound, and residual gallium occur in the weld with the sample holder. S/TEM and energy dispersive X-ray spectrometer (EDS) analysis with a JEOLJEM-2800 microscope at the University of Utah Surface Analysis Laboratory produced dark and light field images and maps of elemental distributions. Images were taken using a nominal probe current of 1.079 nA and an acceleration voltage of 200 kV. The JEOL-2800 microscope is equipped with dual Silicon Drift Detector (SDD) EDS detectors providing a combined solid

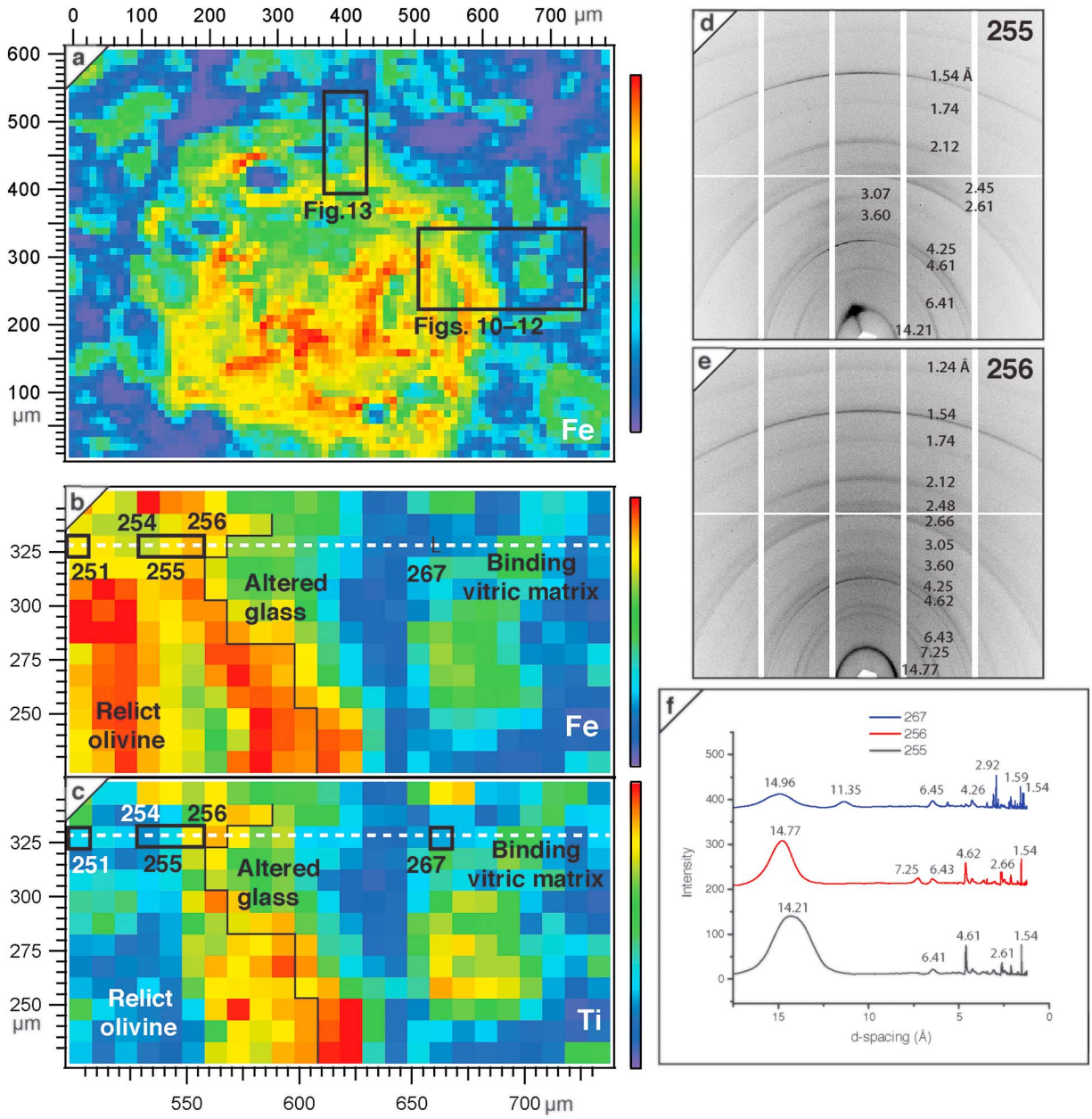

Figure 10. Fractured lapillus, 102.6-m depth, with highly altered olivine and basaltic glass (Figures 7b–7d). (a) Overview, X-ray microfluorescence (µXRF) map, Fe, showing sites of X-ray microdiffraction (µXRD) and micro-computed tomography analyses (Figures 10–13), Raman spectra (Figure 6b), and scanning transmission electron microscopy studies (Figure 12). (b) Grid of µXRD and µXRF (Fe and Ti) analyses, at 10-µm step size, 50 × 125-µm^2 area. Black line marks the approximate boundary between nanocrystalline clay mineral in altered olivine and nanocrystalline clay mineral, analcime, and Al-tobermorite in altered glass. Lower Ti concentrations in the interior of the relict olivine crystal correspond to smaller nontronite (001) interlayer spacing, 13.4 versus 14.5 Å (Figure S5). (d, e) Diffraction images for µXRD analyses #255, the concentrically oriented microstructure (Figure 11), and #256, the feathery fabric, traversed by the focused ion beam lift out (Figure 12). (g) Intensity versus *d* spacing plots for µXRD analyses 255, 256, and 267.

angle of detection of 1.9 for EDS maps. Processing the average of multiple frames, each taken with a 7.85-ms dwell time, was achieved with the Thermo Scientific software NSS Spectral Analysis using a 3 × 3 kernel size, a one-pixel overlap between kernels, and a total pixel count of 65,536.

3.2.5. Raman Spectroscopy

Raman spectra obtained from the FIB lift outs used a confocal laser Olympus BX41 microscope coupled to a Raman spectrometer (Horiba LabRAM HR 800) equipped with a multichannel air-cooled (−70 °C), 1,024 × 256-pixel charge-coupled device array detector and an 1,800-lines-per-millimeter grating. Excitation was

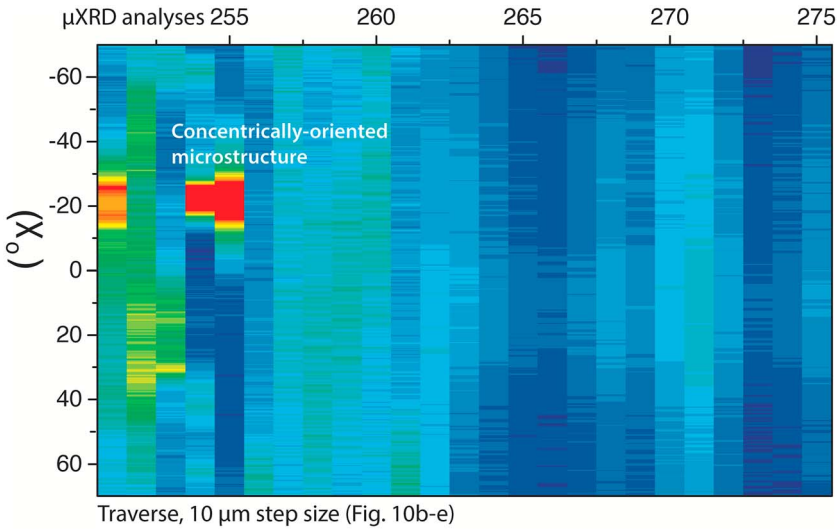

Figure 11. A 250-μm traverse along the *x* axis of the X-ray microdiffraction map (Figures 10 and S5) shows the degrees rotation of the 14.5-Å (001) nontronite *d* spacing around 0°χ in analyses #251–275. Most analyses show no rotation (blue), but analyses #251, #254, and #255 have 14.5-Å (001) *d* spacing crystallographic preferred orientation that rotates through an arch segment of −16°χ to +35°χ (yellow to red). Analysis #255 corresponds to the concentrically layered structure described with scanning transmission electron microscopy and Raman investigations (Figures 6b and 12).

provided by an Ar-ion laser (514 nm) source. Spectra were recorded using a 1-mW laser to avoid laser-induced degradation. The laser beam, focused through a 100X objective, produces approximately 1-μm spot size. Spectral resolution was ~0.3 cm^{-1} per pixel. Instrument accuracy was controlled by repeated use of a silicon wafer calibration standard with a characteristic Raman line at 520.7 cm^{-1}. Spectra were processed using the LabSpec 5 software. The platinum weld/attachment was analyzed to rule out possible contamination; it contains some remains of carbon, but these give completely different spectra than those in the tuff.

3.2.6. Synchrotron Source μCT

Investigations at Advanced Light Source Beamline 8.3.2 examined a fractured lapillus from the 102.6-m depth sample with μCT, also studied with μXRD and μXRF. The analyses used a ~0.6-μm pixel size and a slice spacing ~0.6 μm thick through a narrow, approximately 63 × 952 × 887-$μm^3$ volume. Data were segmented and visualized using Avizo 9 analysis software. Segmentation of the μCT image stack used a histogram-based grayscale thresholding. For certain phases, such as the filled vesicles, segmentation was done manually using the "brush" and interpolation tools. All segmented phases were visualized in 3-D using triangular surface meshes.

4. Results

Integrated microanalytical investigations are reported for glass and olivine components of the tuff at 157.1-, 137.9-, and 102.6-m depths.

4.1. Basaltic Glass Lapillus, 157.1 m

A basaltic lapillus preserves fresh glass, olivine, and plagioclase in its interior and has altered glass rims around vesicles, shown in a petrographic micrograph and corresponding μXRF map (Figures 3a and 3b). The μXRD analysis of the moderate yellow (5Y 8/6) fresh glass (site 1, Figures 3a and 3c) shows no evidence of mineralization. The more Fe-rich vesicle rim (site 4, Figures 3a, 3b, and 3c) is composed of birefringent clinochlore, a magnesium- and iron-rich phyllosilicate with 14-Å (001) interlayer spacing. The platey crystal morphologies are directed orthogonally to the vesicle rim boundary. The diffraction pattern (Figure 3d) indicates an associated crystallographic preferred orientation, shown by intensity variations in the radial direction around the *d* spacing rings. Nearby, the altered glass rim (site 4, Figures 3a, 3b, and 3e) has an inner band (*a*) that is slightly translucent, nonbirefringent, and light olive green (10Y 5/4); an outer band (*b*) that is birefringent and moderate brown (5YR 4/4); and two intervening bands (*c′*) that are opaque,

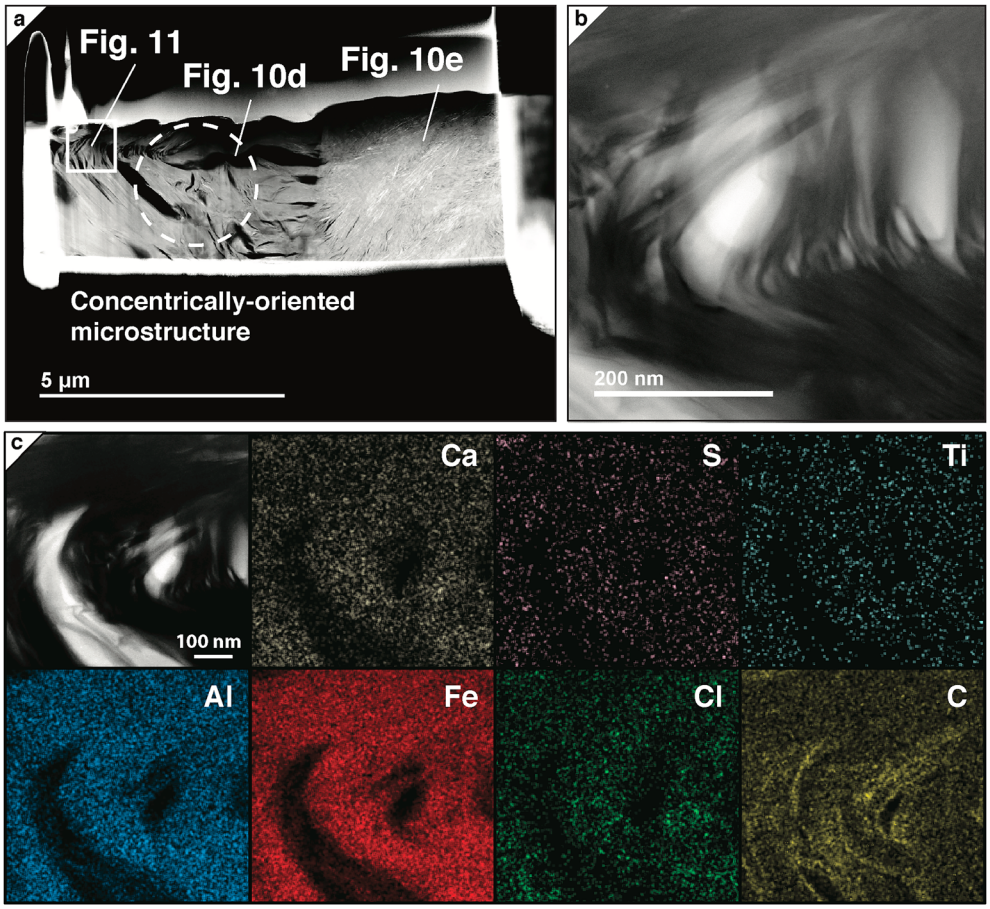

Figure 12. Scanning transmission electron microscopy analyses of nanocrystalline clay mineral within a highly altered olivine crystal, 102.6-m depth (Figures 7b, 10, and 11). (a) Focused ion beam (FIB) lift out, sites of Raman spectra (Figure 7b) and X-ray microdiffraction analyses (Figures 10d–10f and 11 [#255 and #256]). (b) Bright field image, kinked hinge in concentric nanocrystalline clay mineral layers. (c) Scanning transmission electron microscopy-energy dispersive X-ray spectrometer elemental maps. The FIB lift out is oriented perpendicular to the right edge of the olivine crystal (Figure 10), and the axis of rotation in χ is oriented perpendicular to the plane of the lift out.

nonbirefringent, and brownish-black (5YR 2/1). The outermost band (*c′*) has a smooth, sharp interface with the fresh glass. A grid of 105 µXRD analyses (Figure 3e) measured at 3-µm increments along a 30-µm traverse maps the *d* spacings of authigenic minerals in the altered glass. The nonbirefringent bands (*a* and *c*) show weak, nanocrystalline clay mineral *d* spacings. Analcime *d* spacings also occur in the inner band (*a*), and analcime crystals partially fill the adjacent vesicle. The birefringent band (*b*) shows clinochlore *d* spacings. These bands are similar to layers thought to represent the solution interface at successive stages of exposure and chemical alteration with aqueous fluids where incongruent dissolution or leaching of glass produces contemporaneous precipitation of insoluble material at the glass-fluid interface (e.g., Hay & Iijima, 1968; Pauly et al., 2011; Stroncik & Schmincke, 2002; Thorseth et al., 1991). Here, analcime is the principal mineral precipitated from solution. The inner rim (*a*) resembles optically translucent "palagonite," a metastable reaction product on the path to becoming birefringent fibro-palagonite that eventually evolves to smectitic clay mineral (Pauly et al., 2011; Staudigel et al., 1981; Stroncik & Schmincke, 2002). The smectitic mineral occurs in the outer birefringent rim (*b*) as clinochlore. The opaque but nonbirefringent band (*c*) records an intermediate step in this alteration continuum. Note, however, that the presence and composition of a "gel" phase remain unclear.

By contrast, the altered vesicle rims of sites 5, 6, and 7 do not have a smooth interface with the fresh glass (Figure 3a). Instead, innumerable narrow spokes up to 10 µm in length protrude into the glass. (See, also, Figure S1, which shows protrusions around vesicles and fracture surfaces in nearby lapilli). The spokes

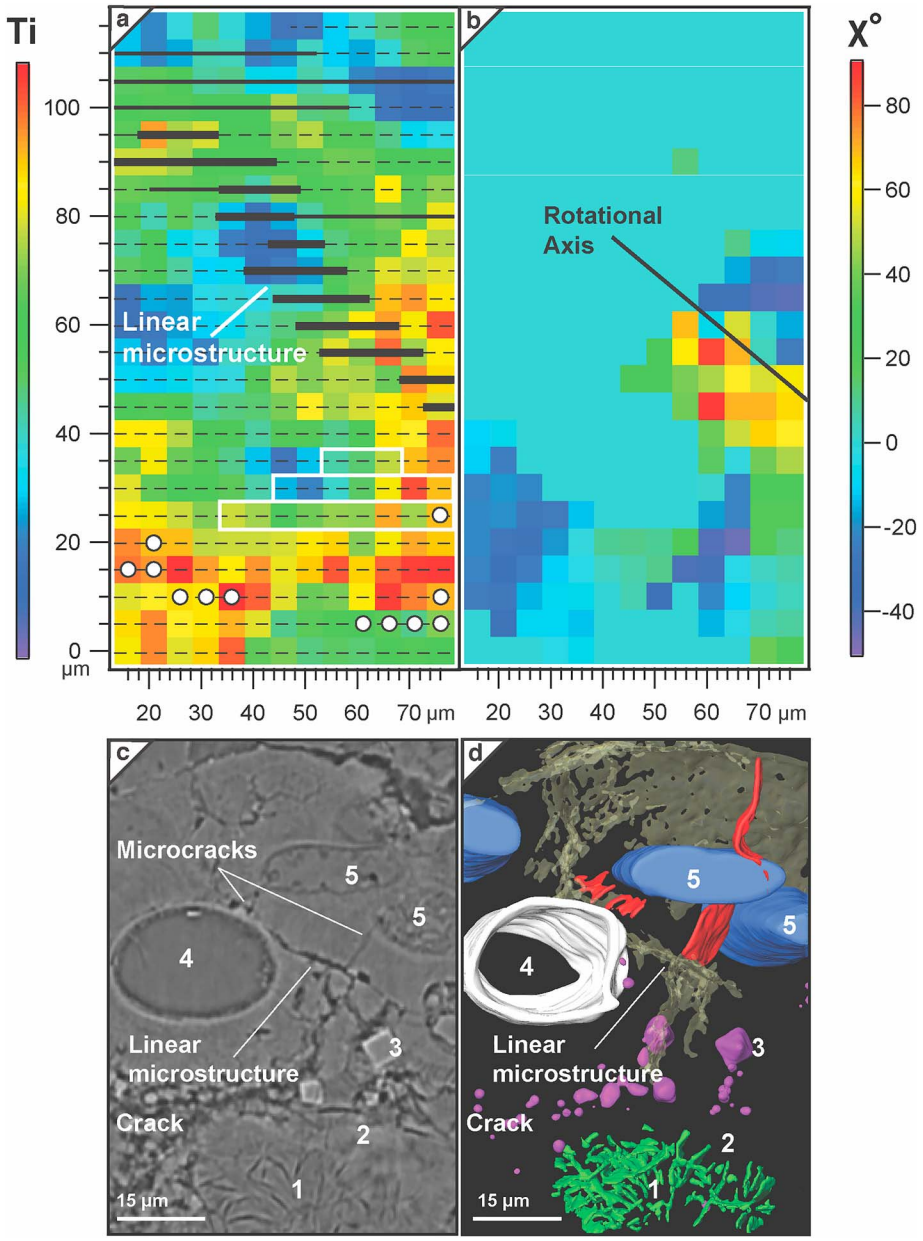

Figure 13. Highly altered basaltic glass of the fractured lapillus, 102.6-m depth (Figures 7b–7d and 10). (a) Grid of X-ray microfluorescence (Ti) analyses, at 5-µm step size, 60 × 120-µm^2 area, showing sites of randomly oriented nanocrystalline clay mineral *d* spacing (dashed lines), a 50 × 20-µm zone of nanocrystalline clay mineral exhibiting crystallographic preferred orientation (heavy black lines), coarse analcime (white outlines), and Al-tobermorite (white circles). (b) The crystallographic preferred orientation of the (001) 14.5-Å peak of the nanocrystalline clay mineral (Figure 13a) rotates over an arch segment (χ) of +50° to −20° along an axis that parallels the linear microstructure (see, also, Figures 7c and 7d). (c, d) Spatial relationships shown by micro-computed tomography analysis: olivine (1, green), Al-tobermorite (2), analcime (3, purple), nanocrystalline clay mineral (gray), empty vesicle (4, white), and vesicles filled with zeolite and Al-tobermorite (5, blue).

resemble narrow, irregular features described as microtubules or channels that are thought to form through endolithic microboring by microorganisms at the boundary between fresh volcanic glass and smectitic clay mineral in diverse basaltic environments (e.g., Fisk et al., 2003; Fisk & McLoughlin, 2013; Furnes et al., 2001; Nikitczuk et al., 2016; Staudigel et al., 2008; Thorseth et al., 1991, 1992). The irregular alteration fronts may also form in the vicinity of sharp, smoothly banded, palagonitic alteration rims (e.g., Fisk et al., 2003, Figure 2; Furnes et al., 2001, Figure 3; Thorseth et al., 1991, Figure 5), Thorseth et al., 1991, Figure 5; Fisk et al.,

Table 1
Nanocrystalline Clay Mineral (Nontronite[a]) d Spacings in Submarine Surtsey Tuff

#43 Vesicle Rim (Figure 5b) 137.9 m	#255 Altered Olivine[b] (Figure 10d) 102.6 m	#256 Altered Olivine (Figure 10e) 102.6 m	Zhou et al. (1992)	Eggleton (1977)	hkl
(Å)	(Å)	(Å)	(Å)	(Å)	
14.98	14.21	14.77	14.73 (100)	15 (100)	001
7.49		7.25	7.56 (10)	7.64	002
	6.41	6.43			
4.61	4.61	4.62	4.98 (10)	5.03	003
	4.25	4.25	4.53 (100)	4.53 (100)	02, 11
3.77	3.60	3.60	3.67 (20)	3.73 (10)	004
2.95	3.07		3.01 (30)	3.02 (30)	005
2.60	2.61	2.66	2.60 (50)	2.61 (40)	20, 13
2.49	2.45	2.48	2.27 (10)		04, 22
	2.12	2.12			
1.74	1.74	1.74	1.72 (20)	1.72 (20)	31, 15, 24
1.54	1.54	1.54	1.52 (80)	1.523 (70)	06, 33
				1.31 (30)	40, 26
	1.24	1.24		1.26 (30)	42, 17, 35

[a]1979 Surtsey nontronite compositions (*Jakobsson & Moore*, 1986), 48-wt% SiO_2, 2.9- to 3.8-wt% Al_2O_3, 28- to 36-wt% FeO, 7- to 17-wt% MgO, 2-wt% CaO, <1-wt% Na_2O, and 1- to 2-wt% K_2O. [b]Crystallographic preferred orientation (Figure 10d).

2003, Figure 2; Walton, 2008, Figures 3 and 5), similar to those at site 4 (Figure 3a). Here, the broad, poorly defined *d* spacings (site 5, Figure 3c) indicate nanocrystalline clay mineral, with broad nontronite *d* spacings for the protrusions as well as for the inner, nonbirefringent altered glass rims.

4.2. Basaltic Glass Lapilli, 137.9 m

A basaltic lapillus, with vesicles containing basaltic fine ash accretions and authigenic Al-tobermorite selvages, records progressive alteration at the micrometer scale (Figure 4). Moderate yellow glass (5Y 8/6) grades into light brown altered glass (5YR 5/6) and to dusky brown altered glass (5YR 2/2). The mineralogical expression of this maturing palagonitization process (Stroncik & Schmincke, 2002) is investigated through μXRD diffraction images (Figure 4b), integrated over 3.5–7.9° 2θ (20- to 9-Å *d* spacing), measured at 5-μm increments along a 180 traverse (Figures 4c and 4d). The μXRD intensity versus *d* spacing plots (Figures 4b and 4e) reveal that weakly altered glass shows little or no (001) reflection (#73–76); weakly matured nanocrystalline clay mineral has a broad, asymmetric (001) reflection (#77, 82–84); and matured nanocrystalline clay mineral has a more symmetric (001) reflection centered at ~14.2 Å (#78–81). This is the smectitic nontronite clay mineral of Jakobsson and Moore (1986). The very finely crystalline nature is shown by the wide, diffuse rings in the diffraction image (Figure 4b). Nontronite has a 2:1 tetrahedral-octahedral-tetrahedral interlayer, separated by water and exchangeable cations. The main Surtsey reflections are similar to nontronite described in 13-Ma Mid-Atlantic Ridge basalt (Zhou et al., 1992), but those determinations were made on hand-picked mineral separates. Here in situ μXRD measurements are spatially coupled with qualitative μXRF maps (Figures 4c and 4d). The analyses indicate that iron and titanium are enriched and calcium depleted in zones of matured nanocrystalline clay mineral, following chemical trends in oceanic basalt-seawater alteration processes (Staudigel & Hart, 1983). Calcium dissolved from the fine accretionary ash and the lapillus formed Al-tobermorite with phillipsite and/or analcime in vesicle environments relatively isolated from hydrothermal fluid flow. The Al-tobermorite (002) interlayer spacing varies from 11.32–11.39 Å, most likely as a function of aluminum content (Jackson et al., 2013).

A larger lapillus appears to have a fresh glass interior, and smooth rims of altered glass 20–50 μm wide surround internal vesicles with mainly phillipsite surface coatings (Figures 2a and 5). However, the μXRD analysis of the moderate yellow (5Y 8/6) clast interior shows a broad, weak, 15.05-Å (001)

reflection, indicative of incipient nanocrystalline clay mineral formation, along with reflections of primary, volcanic plagioclase (Figures 5a and 5b [#7]). By contrast, μXRD analysis of the altered vesicle rim shows a well-defined 14.98-Å (001) reflection and other reflections of nontronite (Figures 5a and 5b [#43], Table 1).

S/TEM dark field images of a FIB lift out of the rim reveal a nanoscale vesicular structure (Figures 5c and 5d), as well as nanoscale subcircular cavities (Figures 5c and 5e). Around the ragged opening of the vesicle (Figure 5d), EDS compositional maps show broad concentrations of iron, diffuse concentrations of calcium and titanium in the relict pore space, and scattered carbon content. An isolated subcircular cavity occurs at the edge of the vesicle, and enlarging the dark field image reveals numerous subcircular nanostructures to the left. These are 5–10 nm in diameter and punctuated by weak carbon concentrations. A grouping of the subcircular cavities spanning about 200 nm shows clumped iron concentrations, increased calcium at the perimeter, dispersed titanium, and little definition in carbon content (Figure 5e). The overall morphology resembles granular textures in porous alteration fronts in palagonitized basalt and basaltic andesite (Furnes et al., 2001; Thorseth et al., 1991) as well as certain subcircular features in ancient seafloor basalt (Alt & Mata, 2000; Fliegel et al., 2012; Knowles et al., 2012), but there are no apparent authigenic mineral fillings. Raman spectra obtained from the lift out (Figures 5c and 6a) are composed of two main broad and overlapping first-order bands at 1,370 cm^{-1} (disorder related) and at 1,580 cm^{-1} (order-related) and second-order bands in the 2,500- to 3,300-cm^{-1} region (overtone scattering; Rahl et al., 2005). These indicate poorly ordered carbonaceous matter of possible biological origin (Bower et al., 2013; Ivarsson et al., 2015). They also indicate that the carbon has degraded and experienced temperatures not exceeding 200 °C (Rahl et al., 2005).

4.3. Basaltic Glass Enrobing Olivine, 137.9 m

A fractured lapillus contains mainly intact olivine crystals, enrobed by altered basaltic glass (Figures 2b and 7a). A complex microcrack partially traverses the olivine and the enclosing glass but does not propagate into the fine ash matrix, suggesting fragmentation during eruption (Colombier et al., 2019; Patel et al., 2013; Wohletz et al., 2013) before final submarine deposition with the surrounding tephra. Several complex subcircular microstructures, 75–200 μm in diameter, occur in the altered glass.

The μXRD and μXRF maps of one such microstructure (Figure 8) illustrate discrete compositional and textural domains: (1) Al-tobermorite, with or without analcime, phillipsite, or minor amicite, a sodic and potassic zeolite ($K_4Na_4[Al_8Si_8O_{32}]\cdot 10H_2O$; site 1; Alberti & Vezzalini, 1979); (2) weakly altered basaltic glass, moderate brown (5YR 4/4, 5YR 3/4), with nanocrystalline clay mineral that is randomly oriented and has a broad (001) reflection at 16–14 Å (site 2) and zeolite; (3) an optically opaque zone, with quenched plagioclase, labradorite in composition (Wenk et al., 1980), and possible gismondine, a calcic zeolite (site 3; Fischer, 1963); (4) a long linear microstructure, about 15 μm in diameter and 60 μm in length, and shorter linear microstructures, moderate brown (5YR 3/4) that occur at the olivine perimeter (sites 4a and 4b; Figures 8b, 8c, 9, and S3); and (5) the mainly intact olivine single crystal with *c* axis oriented tilted steeply left out of the image plane (site 5; Figure S4; Figure S4 (Eggleton, 1984)).

The μXRD analyses indicate that Al-tobermorite occurs as a single phase (with some analcime) in the interior of the subcircular microstructure and with zeolites and nanocrystalline clay mineral in some of the altered glass that rims the microstructure (Figures 8b and S2b). The origins of these complex phase relationships remain unclear. By contrast, there is abundant nanocrystalline clay mineral within the long linear microstructure (site 4b) but little or no Al-tobermorite (Figure S2b). Here the nontronite 4.6-Å (020) reflection exhibits weak crystallographic preferred orientation through an arch segment of −4° to 8°χ (Figure 9a). This is shown by a scattering of blue grid points (8–7°χ) on the left, yellow grid points (2–4°χ) in the center, and dark red grid points on the right (0° to −4°χ). The platey nanocrystalline clay mineral orientations may therefore rotate roughly around an axis that parallels the linear feature, at least in its lower section. Zeolite (amicite) is present in the upper section of the linear microstructure (site 4b), and the crystals also have a preferred orientation (Figure S3). The amicite 2.72-Å *d* spacing, or (−321) plane, rotates through about 18° to −65°χ and appears to be oriented at a high angle to the trend of both the long and shorter linear features. Finally, an irregular dusky yellowish brown (10YR 2/2) zone at the perimeter of the olivine crystal also shows nontronite *d* spacings (site 5, Figures 8b and 8c).

4.4. Basaltic Glass Enrobing Olivine, 102.6 m

A fractured lapillus (Figures 2c and 7b) contains an altered olivine crystal, enrobed by altered basaltic glass (Figures 10–13). At this depth, Jakobsson and Moore (1986) recorded alteration rinds ~50 μm thick on olivine. Here the thin section samples the opaque, dusky yellowish brown (10YR 2/2) alteration rind; only a glimpse of the underlying intact birefringent crystal is exposed. The surrounding altered glass contains several diffuse, dusky yellowish brown (10YR 2/2), nonbirefringent linear microstructures, ≤100 μm in length and 15–25 μm in width, directed more or less radially from vesicles. In epifluorescent light, these appear as narrow, thread-like features with violet (5RP 5/2) autofluorescent illumination (Figure 7c). A microcrack partially traverses the glass rim, and diverse autofluorescent structures occur in the open space between its walls.

Coupled μXRD and μXRF maps at 5-μm incremental step size traverse the relict olivine perimeter, altered glass, and fine ash matrix of the tuff (Figures 10, 12a, and S5). Elevated iron concentrations occur through the altered olivine rind, which is composed principally of nanocrystalline clay mineral (Figure 10b). Elevated titanium concentrations occur in the exterior zone of the altered olivine but are depleted in the interior zone (Figure 10c). In the titanium-enriched external zone, nanocrystalline clay mineral has mainly 14.5-Å (001) *d* spacing (Figures S5d and S5e and Table 1). In the titanium-depleted internal zone, nanocrystalline clay mineral has mainly 13.4-Å (001) *d* spacing (Figures S5d and S5f and Table 1). The ionic radius of $Ti^{+2/3+/4+}$ (0.86, 0.670, and 0.605 Å) is larger than Fe^{+3} (0.69 Å) and Al^{3+} (0.535 Å) and is comparable to Mg^{2+} (0.72 Å; Shannon, 1976). Titanium substitution could therefore produce the larger *c*-axis *d* spacing. Slight calcium enrichment in the zone of relative titanium enrichment, shown by low (Fe+Ti)/Ca (Figure S5b) suggests interaction with the neighboring glass rind, as compared with the internal zone.

A 25-μm traverse across the altered olivine crystal (Figures 10b and 10c) reveals three μXRD analyses, #251, #254, and #255, with strong 14.5-Å (001) crystallographic preferred orientation. In particular, the diffraction image for analysis #255 (Figure 10b) shows intensity variations in nontronite *d* spacings. Figure 11 further indicates the orientations of the 14.5-Å (001) *d* spacings along the #251–275 traverse. In analysis #255, this reflection rotates through an arch segment of 16–35°χ. Analysis #256, by contrast, indicates random orientations (Figures 10e and 11) and a weak 7.25-Å *d* spacing present in some nontronites (Eggleton 1977).

S/TEM analyses at the #255 site reveal morphological layers that wrap concentrically around one another; they also show a sharp kink fold disturbance (Figure 12). Circumferential voids (≤300 nm) separate the layers. The (001) crystallographic preferred orientation (Figures 10d and 11) is aligned within the rotation of the concentric layers. The microstructure, about 20 μm in length and 2–3 μm in width, can be envisioned as similar to a carpet roll of nanocrystalline clay mineral layers that have been locally rumpled in place. The curved layers make a gradational contact with the nanocrystalline clay mineral to the right, which has a feathery, poorly aligned fabric; analysis #256 records randomly nontronite *d* spacing orientations (Figures 10e, 11, and 12a). There is neither a discrete external boundary nor an apparent internal cavity in the concentrically layered structure. S/TEM EDS compositional maps show rather diffuse distributions of calcium, sulfur, titanium, aluminum, and iron yet well-defined carbon concentrations that precisely trace the concentrically layered surfaces and voids (Figures 11 and 12c). Raman spectra (Figures 6b and 12a) show first-order bands at 1,370 and 1,580 cm^{-1} and second-order bands at 2,500–3,300 cm^{-1}, indicating disordered carbonaceous matter (Rahl et al., 2005). In the altered glass enrobing the relict olivine crystal, randomly oriented nanocrystalline clay mineral is accompanied by analcime and by Al-tobermorite at the edge of the lapillus (Figure 10f [#267]).

A larger, more pronounced linear microstructure with concentrically oriented texture occurs within an area of complex microcracks in the altered glass above the relict olivine (Figures 12b, 12c, and 13). There, coupled μXRD and μXRF maps identify strong 14.5-Å (001) crystallographic preferred orientation in nanocrystalline clay mineral within a 25 × 50-μm grid analyzed at 5-μm incremental step size (Figure 13a). The reflections rotate asymmetrically, ~50° to the left and +20° to the right, around an axis that parallels a 100-μm-long linear microstructure (Figure 13b). Violet autofluorescent illuminations occur along its length and in subcircular structures 2–3 μm in diameter at its tips (Figure 7c). Below, a segmented microcrack with high surface roughness traverses the olivine-glass interface and terminates in a large vesicle. Autofluorescent illuminations at a right step in the crack walls range from moderate red (5R 4/6) to grayish orange (10YR 6/4) and very pale blue (5B 8/2). The μXRD analyses (Figure 13a) detect coarse analcime (with pale blue

autofluorescent outlines), salt (NaCl) crystals, fine-grained Al-tobermorite, and nanocrystalline clay mineral.

A μCT reconstruction illustrates spatial relationships among the concentrically oriented linear microstructure, microcracks, and vesicles with and without authigenic mineral fillings (Figures 13c and 13d). The rotational axis of the nanocrystalline clay mineral structure extends from the upper crack surface to the right of a large, empty interior vesicle and then between exterior vesicles filled with authigenic zeolite and Al-tobermorite. The rugged surface of the altered olivine rind bounds the lower crack surface. At least four fracture surfaces traverse the upper margin of the lapillus. Analcime and salt (NaCl) crystals fill the opening along the larger microcrack. The fractures resemble jigsaw textures in lapilli produced by thermal granulation of particle margins during the subaqueous eruption of deposits on Capelhinos and Hunga-Tonga-Hunga Ha'pai volcanoes (Colombier et al., 2019). They suggest that explosive fragmentation and thermal cracking could have occurred during initial quenching in seawater.

5. Discussion

Integrated microanalytical maps of authigenic microstructures in Surtsey submarine basaltic tuff drill core acquired 15 years after eruptions terminated (Jakobsson & Moore, 1982, 1986) illustrate the distribution of nanocrystalline clay mineral and associated zeolite and Al-tobermorite mineral assemblages in the diverse microenvironments of intact and fractured lapilli. At 157.1-m depth, areas in a vesicular lapillus that appear translucent in the plane polarized light may show an amorphous μXRD pattern (Figure 3, site 1), indicating fresh glass. At 137.9-m depth, similarly translucent areas in a vesicular lapillus mainly show a broad, often asymmetric, 16- to 13-Å (001) *d* spacing indicative of incipient nanocrystalline clay mineral (Figure 5b, #7). Slightly less translucent, isotropic rinds around the vesicle perimeters show a more pronounced nanocrystalline clay mineral structure (Figure 5b, #43). In a nearby lapillus with abundant fine ash in vesicles, progressive crystallographic and chemical maturation of the incipient nanocrystalline clay mineral phase in incongruently dissolved glass proceeded in a heterogeneous fashion at 2- to 3-μm spatial resolution; this includes zeolite and Al-tobermorite mineral assemblages near a vesicle surface (Figure 4). The nature of the gel-like, amorphous palagonite alteration product (Stroncik & Schmincke, 2001) in these microstructures remains unclear.

Long-term incubation of sterile, synthetic basaltic glass in the laboratory, at 90 °C and pH ~9 for 900–1,200 days, produces an alteration film composed of a poorly crystalline, nontronite-like clay mineral and amorphous gel (Parruzot et al., 2015). This is similar to the altered glass rind of Figures 5a and 5b (#43). The alteration film is separated from the pristine glass by a film of hydrated glass (Parruzot et al., 2015, Figure 4). From the perspective of palagonitic alteration, these zones are roughly translated as a layer of reactive fluid, a phyllosilicate layer grading to gel-palagonite, and, finally, sideromelane (Pauly et al., 2011, Figure 14). In the experiments, the alteration film is thought to have a passivating effect that may protect the pristine glass from further alteration. Analogous processes may restrict palagonitic alteration to rinds on the surfaces of tephra particles in the subaerial tuff cone at Surtsey (Pauly et al., 2011, Figure 2), yet in the 1979 Surtsey submarine drill core from 65- to 140-m depth, glass in all but large lapilli has mainly altered to a suite of authigenic minerals (Jakobsson & Moore, 1986, Figure 6).

5.1. Subcircular Nanoscale Cavities

Discrete nanoscale subcircular cavities in the altered vesicle rim of a basaltic lapillus at 137.9-m depth have 10- to 25-nm diameters (Figure 5). These diameters are smaller than those of 100- to 500-nm granular features in ancient pillow basalts (Alt & Mata, 2000; Fliegel et al., 2012; Knowles et al., 2012). Those granular (and tubular) structures have a 10- to 30-nm-thick, leached layer at the interface with the fresh glass. This annular alteration rim is depleted in Mg, Fe, Ca, and Na (Alt & Mata, 2000; Fliegel et al., 2012; Knowles et al., 2012) or enriched in silica (Benzerara et al., 2007), and the alteration cavity is filled with phyllosilicate mineral. In the very young Surtsey nanoscale cavities, however, no alteration rind, clay mineral infill, or trace of narrow appendages occur. Instead, calcium is enriched along perimeters rather than depleted and the glass is transformed into nanocrystalline clay mineral (Figures 5d and 5e). The dissolution mechanism(s) remain unclear. Elemental carbon concentrations outline cavity perimeters and Raman spectra indicate poorly ordered carbonaceous matter (Figures 5c and 6a), similar to that which is used as an indicator for the biological origin of putative fossilized structures (Bower et al., 2013; Ivarsson et al., 2015).

5.2. Concentrically Oriented Linear Microstructures

Concentric layers of nanocrystalline clay mineral that contain a rotational component of crystallographic preferred orientation occur in a 20-μm-long linear microstructure mapped in altered olivine at 102.6-m depth (Figures 10–12 and S5). The μXRD analyses detect a rotation of 20°χ in the crystallographic preferred orientation of the 14.5-Å (001) nanocrystalline clay mineral *d* spacing within the linear structure (Figures 10d and 11). Successive rotation of the orientation of the sample with respect to the beamline detector would, however, be required to detect the full concentric structure. Elemental carbon concentrations explicitly trace the morphology of the curved layers of nanocrystalline clay mineral (Figure 12). These are associated with Raman spectra at 1,370 and 1,580 cm^{-1} that are indicative of poorly ordered carbonaceous matter (Figure 6b; Bower et al., 2013; Ivarsson et al., 2015) and associated with vibrational bending of amino acid ring structures (Fisk et al., 2003). Possible abiotic sources could be carbonate minerals produced through fluid-rock interactions, such as calcite, metastable vaterite, or hydrotalcite (Benzerara et al., 2007), yet these are not present in the μXRD patterns (Figures 10d–10f).

The morphology of this linear microstructure and its diffuse, gradational contact with surrounding nanocrystalline clay mineral in the relict olivine crystal has little or no resemblance to the microtunnels, microchannels, and microborings commonly described in oceanic basalts (e.g., Fisk & McLoughlin, 2013). These features, which develop through abiotic and biotic microcorrosion of volcanic glass, have discrete walls that bound an internal cavity; the tube is eventually sealed through authigenic mineral precipitation (Staudigel et al., 2008; Thorseth et al., 1992). The morphology does, however, resemble that of a layered chlorite-smectite microstructure, about 1 μm in diameter and 2 μm in length, adjacent to nanoporous maghemite in ≤500-ka Krafla basalt, Iceland (Oliva-Urcia et al., 2011). This microstructure and the concentrically arranged, phyllosilicate packets in the annular nanostructures of pillow basalts (Alt & Mata, 2000; Fliegel et al., 2012; Knowles et al., 2012) could, potentially, be organized with crystallographic preferred orientation, yet no explanation currently exists for how and why these features develop.

Longer linear microstructures in altered glass at 137.9- and 102.6-m depth also contain concentrically oriented crystallographic preferred orientation of nanocrystalline clay mineral *d* spacings. In the fractured lapillus at 102.6-m depth, the longitudinal axis of rotation of the 14.5-Å (001) *d* spacing exactly parallels a thread-like lineation about 100 μm in length, detected through violet UV-excited native fluorescence (Figure 13). Fractures surround the linear microstructure, suggesting that seawater may have infiltrated the clast after submarine deposition. Intense fluorescence that is variable in color also occurs in association with analcime and salt crystals within one of these microcracks. Although organic matter may be present (Bhartia et al., 2010; Fisk et al., 2003), the origins of this native fluorescence, as well as the more complex concentrically oriented linear microstructure in the fractured lapillus at 137.9-m depth remain unclear (Figures 8 and 9). It is not known, for example, whether the arrangement of the nanocrystalline nontronite and zeolite orientations follows an annular or a spiral-shaped, helicoidal pattern. The crystallographic resemblance to 20-cm-diameter, nontronite-bearing tube-like structures on Mashi seamount in the Galapagos Islands (Lubetkin et al., 2018) remains to be determined.

5.3. A Ramified Interface With Fresh Glass

Fine protrusions around altered vesicle rinds in a basaltic lapillus at 157.1-m depth (Figure 3, site 5) show a resemblance to microchannels that occur at the boundary of fresh and altered glass in older basalts. These are illustrated, for example, by Hawaii Scientific Drilling Program borehole samples where seawater remains present and both clay mineral and microbial cells have been detected (Fisk et al., 2003, Figure 2). Neighboring lapilli in the Surtsey tuff sample at 157.1-m depth contain innumerable examples of these irregular alteration fronts (Figure S1). This sample occurs within the lower temperature zone of the Surtsey hydrothermal system, ≤83 °C in 1980, near the preeruption seafloor where bacterial and archæal communities were detected in borehole fluids in 2009 (Marteinsson et al., 2015; Figure 1). This raises the possibility that microbial processes could, potentially, have played a role in the alteration of the freshly erupted basaltic tephra. These topics will be considered in future investigations of the 2017 Surtsey drill core samples and basaltic glass and olivine incubation experiments within a subsurface borehole observatory (Jackson et al., 2019; Türke et al., 2019).

5.4. The Role of Microenvironments

The coupled μXRD and μXRF maps of the submarine lapilli (Figures 3, 4, 8, 10, and 12) provide an introductory foundation for future descriptions of basaltic glass alteration in Surtseyan deposits using thermodynamic and kinetic principles and models for evaluating glass-fluid interactions (e.g., Jantzen et al., 2010, 2017). At lower temperature and depth, 157.1 m, the progressive organization of nanocrystalline clay mineral in glass is confined to banded rinds of isotropic or birefringent smectitic clay mineral (Figure 3). By contrast, at 137.9-m depth, the rapid, initial incongruent dissolution of glass produces alkaline solutions from which abundant authigenic mineral cements precipitate (Figure 4). Al-tobermorite selvages 40–70 μm thick, for example, crystallized from highly alkaline fluids in vesicles partially filled with reactive fine ash and isolated from larger-scale fluid flow. The progressive aging and maturation of hydrated gel in the leached glass framework is recorded by incipient mineralization to nanocrystalline clay mineral (Figure 4e, #73–76) and nontronite (Figure 4e, #78–80), accompanied by higher (Fe+Ti)/Ca concentrations (Figures 4c and 4d). At increased temperature and depth, 102.6 m, partitioning of titanium in altered glass and olivine influenced the crystallographic properties of nanocrystalline nontronite (Figures 10 and S5 and Table 1).

Rates of glass and crystal alteration at Surtsey during the 15 years that elapsed after eruptions terminated were influenced at the larger scale by the temperature and composition of leaching and fluids (Figure 1), as well as the evolving porosity and permeability characteristics of the tephra and tuff (Jakobsson & Moore, 1986; Oddson, 1982). The results of the integrated microanalytical maps indicate that rates of alteration are also driven by fine-scale processes in microenvironments: internal vesicles in lapilli (Figures 3 and 5), altered fine ash accretions in vesicles (Figure 4), subcircular microstructures (Figure 8), microcracks in fractured lapilli (Figures 10–13), and the altered fine ash matrix (Figures 10b and 10c). The maps indicate that glass alteration proceeds differently within the same sample as a function of micrometer-scale changes. These include the exposed surface area, the volume, flow and changing composition of the leaching fluid (Jantzen et al., 2010), and the poorly understood processes that occur in subcircular and linear microstructures. The subcircular microstructure at 137.9-m depth, for example, illustrates the complex growth of zeolite and Al-tobermorite crystal assemblages in a relict cavity (Figure 8, site 1) and in the leached glass framework (Figure 8, site 2). The growth of authigenic minerals in relict pore space may be produced by resumption of dissolution in glass or crystals, which then lowers the overall free energy of the system (Jantzen et al., 2017).

These fine-scale systems can be envisioned as chemically dynamic microenvironments, similar to those in ancient Roman marine harbor concretes with trachytic volcanic glass aggregates. There, the long-term growth of mineral cements has produced authigenic mineral cycling from zeolite to Al-tobermorite phases for 2,000 years (Jackson et al., 2017). The dynamic and probably nonequilibrium nature of the alteration microenvironments in Surtsey tuff and the ongoing cementitious processes recorded by these rocks will provide an important geologic analog for extremely durable concretes with volcanic and synthetic glass aggregates.

6. Summary and Conclusions

Multiple high-resolution microanalyses have been applied to three specimens of submarine basalt drill core collected in 1979 from Surtsey volcano, 15 years after eruptions terminated. The resulting micrometer-scale maps build on previous investigations of the drill core samples (Jakobsson & Moore, 1982, 1986). They provide fine-scale observations of the processes that control the conversion of very young oceanic basaltic glass and olivine into authigenic mineral assemblages in an exceptionally well-constrained, natural hydrothermal laboratory.

Depth and temperature in the submarine hydrothermal system influence rates of glass alteration, so that in larger lapilli, fresh glass may be preserved at 157.1 m (Figure 3), weakly altered at 137.9 m (Figure 5) and strongly altered at 102.6-m depth (Figure 10), confirming the observations of Jakobsson and Moore (1986). In addition, microanalytical maps indicate that nanometer- and micrometer-scale environments in vesicular and fractured lapilli played an important role in the initial organization of authigenic mineral assemblages in altered glass and olivine crystals. The maps provide new mineralogical clarity to palagonitic alteration processes and the dynamic microenvironments of alteration in young oceanic basalt.

At 157.1-m depth, fine-scale protrusions around altered vesicle rinds in a basaltic lapillus (Figures 3 and S1) resemble biomediated microchannels that occur along irregular alteration fronts between fresh and altered glass in older basalts (e.g., Furnes et al., 2001, Figure 4; Fisk et al., 2003, Figure 2; Walton, 2008, Figures 3 and 5). Bacterial and archaeal communities were detected in borehole fluids near this depth in 2009 (Marteinsson et al., 2015), suggesting that microbial processes could, potentially, have played a role in the alteration of freshly erupted basaltic tephra near the preeruption seafloor. By contrast, linear microstructures with complex nanocrystalline clay mineral and zeolite texture represent microcorrosion of basaltic glass and olivine crystals in fractured lapilli, yet these have not been described in previous literature (Figures 9–11). Crystallographic preferred orientation rotates around the long axis of these opaque, isotropic features. Nanoscale carbon selvages precisely trace the layered surfaces and voids of one example (Figure 12). Raman spectra indicative of poorly organized carbonaceous matter of possible biological origin are associated with these layers and with nanoscale subcircular cavities in altered glass at 137.9-m depth (Figures 5 and 6). The origins of these structures remain unclear. They may represent delicate features that vanish when successive responses to changing environmental conditions overprint initial, posteruptive alteration processes in oceanic basalts.

The alteration of basalt, including glass and olivine, in the oceanic crust plays a key role in the ongoing processes that influence in the crustal geochemistry of Earth. The alteration microenvironments and complex mineral texture in the very young submarine basalt of Surtsey volcano provides a new reference framework for understanding the earliest stages of ocean-basalt interactions and the power of modern instrumental techniques to describe the results of these processes.

Acknowledgments

We thank B. Vandevener and R. Polson, Nanofabrication Laboratory, University of Utah; B. Bowen, University of Utah, Department of Geology and Geophysics; Y. Li, Xi'an Jiaotong University, China; H.-R. Wenk and T. Teague, Department of Earth and Planetary Sciences, University of California, Berkeley; and J. D. L. White, University of Otago, New Zealand, for research support. The article benefited from discussion and reviews from T. W. Sisson, A. W. Walton, and H. Staudigel. Samples were provided from the 1979 Surtsey drill core archive at the Iceland Institute of Natural History, Garðabær, Iceland. Research data are available through a data repository at University of Utah, https://doi.org/10.7278/S50D-VJND-8V00. The College of Mines and Earth Sciences at University of Utah provided funding support. This research made use of University of Utah USTAR shared facilities supported, in part, by the MRSEC Program of NSF under Award DMR-1121252. Data acquired at Advance Light Source beamlines 12.3.2. and 8.3.2. This is a Department of Energy Office of Science User Facility under contract DE-AC02-05CH11231. Any use of trade, firm, or product names is for descriptive purposes only and does not imply endorsement by the U.S. Government.

References

Alberti, A., & Vezzalini, G. (1979). The crystal structure of amicite, a zeolite. *Acta Crystallographica*, *B35*, 2866–2869.

Alt, J. C., & Mata, P. (2000). On the role of microbes in the alteration of submarine basaltic glass: A TEM study. *Earth and Planetary Science Letters*, *181*(3), 301–313. https://doi.org/10.1016/S0012-821X(00)00204-1

Bengtson, S., Rasmussen, B., Ivarsson, M., Muhling, J., Broman, C., Marone, F., & Stampanoni, M. (2017). Fungus-like mycelial fossils in 2.4 billion-year-old vesicular basalt. *Nature Ecology and Evolution*, *1*, 0141.

Benzerara, K., Menguy, N., Banerjee, N. R., Tyliszczak, T., Brown, G. E. Jr., & Guyot, F. (2007). Alteration of submarine basaltic glass from the Ontong Java Plateau: A STXM and TEM study. *Earth and Planetary Science Letters*, *260*(1-2), 187–200. https://doi.org/10.1016/j.epsl.2007.05.029

Bhartia, R., Salas, E. C., Hug, W. F., Reid, R. D., Lane, A. L., Edwards, K. J., & Nealson, K. H. (2010). Label-free bacterial imaging with deep-UV-laser-induced native fluorescence. *Applied Environmental Microbiology*, *76*(21), 7231–7237. https://doi.org/10.1128/AEM.00943-10

Bower, D. M., Steele, A., Fries, M. D., & Kater, L. (2013). Micro Raman spectroscopy of carbonaceous material in microfossils and meteorites: Improving a method for life detection. *Astrobiology*, *13*(1), 103–113. https://doi.org/10.1089/ast.2012.0865

Colombier, M., Scheu, B., Kueppers, U., Cronin, S. J., Mueller, S. B., Hess, K. U., et al. (2019). In situgranulation by thermal stress during subaqueous volcanic eruptions. *Geology*, *47*(2), 179–182. https://doi.org/10.1130/G45503.1

Crovisier, J.-L., Advocat, T., & Dussossoy, J.-L. (2003). Nature and role of natural alteration gels formed on the surface of ancient volcanic glasses (Natural analogs of waste containment glasses). *Journal of Nuclear Materials*, *321*(1), 91–109. https://doi.org/10.1016/S0022-3115(03)00206-X

Eggleton, R. A. (1977). Nontronite: Chemistry and X-ray diffraction. *Clay Minerals*, *12*(3), 181–194. https://doi.org/10.1180/claymin.1977.012.3.01

Eggleton, R. A. (1984). Formation of iddingsite rims on olivine: A transmission microscope study. *Clays and Clay Minerals*, *32*(1), 1–11. https://doi.org/10.1346/CCMN.1984.0320101

Fischer, K. (1963). The crystal structure determination of the zeolite gismondite, $CaAl_2Si_2O_8$. *American Mineralogist*, *48*(3), 664–672.

Fisk, M. R., & McLoughlin, N. (2013). Atlas of alteration textures in volcanic glass from the ocean basins. *Geosphere*, *39*(2), 317–341.

Fisk, M. R., Storrie-Lombardi, M. C., Douglas, S., Popa, R., & Di Meo-Savoie, C. (2003). Evidence of biological activity in Hawaiian subsurface basalts. *Geochemistry Geophysics Geosystems*, *4*(12), 1103. https://doi.org/10.1029/2002GC000387

Fliegel, D., Knowles, E., Wirth, R., Templeton, A., Staudigel, H., Muehlenbachs, K., & Furnes, H. (2012). Characterization of alteration textures in Cretaceous oceanic crust (pillow lava) from the N-Atlantic (DSDP Hole 418A) by spatially-resolved spectroscopy. *Geochimica and Cosmochimica Acta*, *96*, 80–93. https://doi.org/10.1016/j.gca.2012.08.026

Furnes, H. (1978). Element mobility during palagonitization of a subglacial hyaloclastite in Iceland. *Chemical Geology*, *22*(3), 249–264. https://doi.org/10.1016/0009-2541(78)90034-7

Furnes, H., Staudigel, H., Thorseth, I. H., Torsvik, T., Muehlenbachs, K., & Tumyr, O. (2001). Bioalteration of basaltic glass in the oceanic crust. *Geochemistry Geophysics Geosystems*, *2*(8). https://doi.org/10.1029/2000GC000150

Gislason, S. R., & Oelkers, E. H. (2003). Mechanism, rates, and consequences of basaltic glass dissolution: II. An experimental study of the dissolution rates of basaltic glass as a function of pH and temperature. *Geochimica and Cosmochimica Acta*, *67*(20), 3817–3832. https://doi.org/10.1016/S0016-7037(03)00176-5

Hay, R. L., & Iijima, A. (1968). Nature and origin of palagonite tuffs of the Honolulu Group on Oahu, Hawaii. In R. R. Coats, R. L. Hay, & C. A. Anderson (Eds.), *Studies in volcanology*, *Geological of Society America Memoir*, (Vol. 116, pp. 331–376). https://doi.org/10.1130/MEM116

Ivarsson, M., Bengtson, S., Skogby, H., Lazor, P., Broman, C., Belivanova, V., & Marone, F. (2015). A fungal-prokaryotic consortium at the basalt-zeolite interface in subseafloor. *PLoS ONE*, *10*(10). https://doi.org/10.1371/journal.pone.0140106

Ivarsson, M., Broman, C., Lindbolm, S., & Holm, N. G. (2009). Fluid inclusions as a tool to constrain the preservation conditions of subseafloor cryptoendoliths. *Planetary and Space Science*, *57*(4), 477–490. https://doi.org/10.1016/j.pss.2008.09.006

Jackson, M. D., Gudmundsson, M. T., Bach, W., Cappelletti, P., Coleman, N. J., Ivarsson, M., et al. (2015). Time-lapse characterization of hydrothermal seawater and microbial interactions with basaltic tephra at Surtsey Volcano. *Scientific Drilling*, *20*, 51–58. https://doi.org/10.5194/sd-20-51-2015

Jackson, M. D., Gudmundsson, M. T., Weisenberger, T. B., Rhodes, J. M., Stefánsson, A., Kleine, B. I., et al. (2019). SUSTAIN drilling at Surtsey volcano, Iceland, tracks hydrothermal and microbiological interactions in basalt 50 years after eruption. *Scientific Drilling*, *25*, 35–46. https://doi.org/10.5194/sd-25-35-2019

Jackson, M. D., Moon, J., Gotti, E., Taylor, R., Chae, S. R., Kunz, M., et al. (2013). Material and elastic properties of Al-tobermorite in ancient Roman seawater concrete. *Journal of the American Ceramic Society*, *96*(8), 2598–2606. https://doi.org/10.1111/jace.12407

Jackson, M. D., Mulcahy, S. R., Chen, H., Li, Y., Li, Q., Cappelletti, P., & Wenk, H.-R. (2017). Phillipsite and Al-tobermorite produced by cementitious water-rock reactions in Roman marine concrete. *American Mineralogist*, *102*(7), 1435–1450. https://doi.org/10.2138/am-2017-5993CCBY

Jakobsson, S. P. (1978). Environmental factors controlling the palagonitization of the Surtsey tephra, Iceland. *Bulletin of the Geological Society of Denmark*, *27*, 91–105.

Jakobsson, S. P., & Moore, J. G. (1982). The Surtsey research drilling project of 1979. *Surtsey Research Progress Report*, *9*, 76–93.

Jakobsson, S. P., & Moore, J. G. (1986). Hydrothermal minerals and alteration rates at Surtsey volcano, Iceland. *Geological Society of America Bulletin*, *97*(5), 648–659. https://doi.org/10.1130/0016-7606(1986)97<648:HMAARA>2.0.CO;2

Jakobsson, S. P., Thors, K., Vésteinsson, Á. T., & Ásbjörnsdóttir, L. (2009). Some aspects of the seafloor morphology at Surtsey volcano: The new multibeam bathymetric survey of 2007. *Surtsey Research*, *12*, 9–20.

Jantzen, C. M., Brown, K. J., & Pickett, J. M. (2010). Durable glass for thousands of years. *International Journal of Applied Glass Science*, *1*(1), 38–62. https://doi.org/10.1111/j.2041-1294.2010.00007.x

Jantzen, C. M., Trivelpiece, C. L., Crawford, C. L., Pareizs, J. M., & Pickett, J. M. (2017). Accelerated Leach Testing of Glass (ALTGLASS): II. Mineralization of hydrogels by leachate strong bases. *International Journal of Applied Glass Science*, *8*(1), 84–96. https://doi.org/10.1111/ijag.12264

Kashefi, K., & Lovley, D. R. (2003). Extending the upper temperature limit for life. *Science*, *301*(5635), 934. https://doi.org/10.1126/science.1086823

Knowles, E., Worth, R., & Templeton, A. (2012). A comparative analysis of potential biosignatures in basalt glass by FIB-TEM. *Chemical Geology*, *330–331*, 165–175.

Kruber, C., Thorseth, I. H., & Pederson, R. B. (2008). Seafloor alteration of basaltic glass, texture, chemistry and endolithic organisms. *Geochemistry Geophysics Geosystems*, *9*, Q12029. http://DOI, https://doi.org/10.1029/2008GC002199

Lubetkin, M., Carey, S., Kelley, K. A., Robert, G., Cornell, W., Raineault, N., et al. (2018). Nontronite-bearing tubular hydrothermal deposits from a Galapagos seamount. *Deep-Sea Research Part II*, *150*, 181–194. https://doi.org/10.1016/j.dsr2.2017.09.017

Marteinsson, V., Klonowski, A., Reynisson, E., Vannier, P., Sigurdsson, B. D., & Ólafsson, M. (2015). Microbial colonization in diverse surface soil types in Surtsey and diversity analysis of its subsurface microbiota. *Biogeosciences*, *12*(4), 1191–1203. https://doi.org/10.5194/bg-12-1191-2015

McLoughlin, N., Staudigel, H., Furnes, H., Eickmann, B., & Ivarsson, M. (2010). Mechanisms of microtunneling in rock substrates: distinguishing endolithic biosignatures from abiotic microtunnels. *Geobiology*, *8*, 245–255. https://doi.org/10.1111/j.1472-4669.2010.00243.x

Moore, J. G. (1966). Rate of palagonitization of submarine basalt adjacent to Hawaii. *United States Geological Survey Professional Paper*, *550-D*, 163–171.

Nikitczuk, M. C. P., Schmidt, M. E., & Flemming, R. L. (2016). Candidate microbial ichnofossils in continental basaltic tuffs of central Oregon, USA: Expanding the record of endolithic microborings. *Geological Society of America Bulletin*, *128*(7/8), 1270–1285.

Oddson, B. (1982). Rock quality designation and drilling rate correlated with lithology and degree of alteration in volcanic rocks from the Surtsey 1979 drill hole. *Surtsey Research Progress Reports*, *9*, 94–97.

Oelkers, E. H., & Gislason, S. R. (2001). The mechanism, rates and consequences of basaltic glass dissolution: I. An experimental study of the dissolution rates of basaltic glass as a function of aqueous Al, Si and oxalic concentration at 25°C and pH 3 and 11. *Geochimica and Cosmochimica Acta*, *65*(21), 3671–3681. https://doi.org/10.1016/S0016-7037(01)00664-0

Oliva-Urcia, B., Kontny, A., Vahle, C., & Schleicher, A. M. (2011). Modification of the magnetic mineralogy in basalts due to fluid–rock interactions in a high-temperature geothermal system (Krafla, Iceland). *Geophysical Journal International*, *186*(1), 155–174. https://doi.org/10.1111/j.1365-246X.2011.05029.x

Parruzot, B., Rébiscoul, D., & Gin, S. (2015). Long-term alteration of basaltic glass: Mechanisms and rates. *Geochimica and Cosmochimica Acta*, *154*, 28–48. https://doi.org/10.1016/j.gca.2014.12.011

Patel, A., Manga, M., Carey, R. J., & Degruyter, W. (2013). Effects of thermal quenching on mechanical properties of pyroclasts. *Journal of Volcanology and Geothermal Research*, *258*, 24–30. https://doi.org/10.1016/j.jvolgeores.2013.04.001

Pauly, B. D., Schiffman, P., Zierenberg, R. A., & Clague, D. A. (2011). Environmental and chemical controls on palagonitization. *Geochemistry Geophysics Geosystems*, *12*, Q12017. https://doi.org/10.1029/2011GC003639

Peacock, M. A. (1926). The petrology of Iceland, part 1: The basic tuffs. *Transactions of the Royal Society of Edinburgh*, *55*, 53–76.

Prieur, D., & Marteinsson, V. T. (1998). Prokaryotes living under elevated hydrostatic pressure. *Advances in Biochemical Engineering/Biotechnology*, *61*, 23–35. https://doi.org/10.1007/BFb0102288

Rahl, J. M., Anderson, K. M., Brandon, M. T., & Fassoulas, C. (2005). Raman carbonaceous material thermometry of low-grade metamorphic rocks: Calibration and application to tectonic exhumation in Crete, Greece. *Earth and Planetary Science Letters*, *240*(2), 339–354. https://doi.org/10.1016/j.epsl.2005.09.055

Salas, E. C., Bhartia, R., Anderson, L., Hug, W. F., Reid, R. D., Iturrino, G., & Edwards, K. G. (2015). In situ detection of microbial life in the deep biosphere in igneous ocean crust. *Frontiers of Microbiology*, *6*(120), 1–8.

Schipper, C. I., Jakobsson, S. P., White, J. D. L., Palin, J. M., & Bush-Marcinowski, T. (2015). The Surtsey magma series. *Scientific Reports*, *5*(1), 11498. http://doi, https://doi.org/10.1038/srep11498

Shannon, S. D. (1976). Revised effective ionic radii and systematic studies of interatomic distances in halides and chaleogenides. *Acta Crystallographica*, *32*, 751.

Stan, C. V., & Tamura, N. (2018). Synchrotron X-ray microdiffraction and fluorescence imaging of mineral and rock samples. *Journal of Visualized Experiments*, *136*. https://doi.org/10.3791/57874

Staudigel, H., Furnes, H., & de Wit, M. (2015). Paleoarchean trace fossils in altered volcanic glass. *Proceedings of the National Academy of Sciences*, *112*(22), 6892–6897. https://doi.org/10.1073/pnas.1421052112

Staudigel, H., Furnes, H., McLoughlin, N., Banerjee, N. R., Connell, L. B., & Templeton, A. (2008). 3.5 billion years of glass bioalteration: Volcanic rocks as a basis for microbial life? *Earth Sciences Reviews*, *89*(3-4), 156–176. https://doi.org/10.1016/j.earscirev.2008.04.005

Staudigel, H., & Hart, S. R. (1983). Alteration of basaltic glass: Mechanisms and significance for the oceanic crust-seawater budget. *Geochimica and Cosmochimica Acta*, *47*(3), 337–350. https://doi.org/10.1016/0016-7037(83)90257-0

Staudigel, H., Hart, S. R., & Richardson, S. H. (1981). Alteration of the ocean crust: Processes and timing. *Earth and Planetary Science Letters*, *52*(2), 311–327. https://doi.org/10.1016/0012-821X(81)90186-2

Stéfansson, V., Axelsson, G., Sigurdsson, O., Gudmundsson, G., & Steingrimsson, B. (1985). Thermal condition of Surtsey. *Journal of Geodynamics*, *4*(1-4), 91–106. https://doi.org/10.1016/0264-3707(85)90054-7

Stroncik, N. A., & Schmincke, H.-U. (2001). Evolution of palagonite: Crystallization, chemical changes, and element budget. *Geochemistry Geophysics Geosystems*, *2*(7). http://doi.org/10.1029/2000GC000102

Stroncik, N. A., & Schmincke, H.-U. (2002). Palagonite—A review. *International Journal of Earth Science*, *91*(4), 680–697. https://doi.org/10.1007/s00531-001-0238-7

Tamura, N. (2014). XMAS: A versatile tool for analyzing synchrotron microdiffraction data. In G. Ice, & B. Barabash (Eds.), *Strain and dislocation gradients from diffraction*, (Vol. 4, pp. 125–155). Singapore: World Scientific. https://doi.org/10.1142/9781908979636_0004

Tamura, N., Kunz, M., Chen, K., Celestre, R. S., MacDowell, A. A., & Warwick, T. (2009). A superbend X-ray microdiffraction beamline at the Advanced Light Source. *Materials Science and Engineering A*, *524*(1–2), 28–32. https://doi.org/10.1016/j.msea.2009.03.062

Thórarinsson, S. (1967). *Surtsey, The New Island in the North Atlantic*. New York: The Viking Press.

Thorseth, I. H., Furnes, H., & Heldal, M. (1992). The importance of microbiological activity in the alteration of natural basaltic glass. *Geochimica and Cosmochimica Acta*, *56*(2), 845–850. https://doi.org/10.1016/0016-7037(92)90104-Q

Thorseth, I. H., Furnes, H., & Tumyr, O. (1991). A textural and chemical study of Icelandic palagonite of varied composition and its bearing on the mechanism of the glass-palagonite transformation. *Geochimica and Cosmochimica Acta*, *55*(3), 731–749. https://doi.org/10.1016/0016-7037(91)90337-5

Thorseth, I. H., Pederson, R. B., & Christie, D. M. (2003). Microbial alteration of 0-30-Ma seafloor and sub-seafloor basaltic glasses from the Australian Antarctic Discordance. *Earth and Planetary Science Letters*, *215*(1-2), 237–247. https://doi.org/10.1016/S0012-821X(03)00427-8

Thorseth, I. H., Torsvik, T., Torsvik, V., Daae, F. L., & Pedersen, R. B. (2001). Diversity of life in ocean floor basalt. *Earth and Planetary Science Letters*, *194*(1-2), 31–37. https://doi.org/10.1016/S0012-821X(01)00537-4

Torsvik, T., Furnes, H., Muehlenbachs, K., Thorseth, I. H., & Tumyr, O. (1998). Evidence for microbial activity at the glass-alteration interface in oceanic basalts. *Earth and Planetary Science Letters*, *162*(1-4), 165–176. https://doi.org/10.1016/S0012-821X(98)00164-2

Türke, A., Jackson, M. D., Bach, W., Kahl, W.-A., Grzybowski, B., Marshall, B., et al. (2019). Design of the subsurface observatory at Surtsey Volcano, Iceland. *Scientific Drilling*, *25*, 57–62. https://doi.org/10.5194/sd-25-57-2019

Türke, A., Ménez, B., & Bach, W. (2018). Comparing biosignatures in aged basaltic glass from North Pond, Mid-Atlantic ridge and Louisville seamount trail, off New Zealand. *PLoS ONE*, *13*(2). https://doi.org/10.1371/journal.pone.0190053

Walton, A. W. (2008). Microtubules in basalt glass from Hawaii Scientific Drilling Project #2 phase 1 core and Hilina slope, Hawaii: Evidence of the occurrence and behavior of endolithic microorganisms. *Geobiology*, *6*(4), 351–364. https://doi.org/10.1111/j.1472-4669.2008.00149.x

Walton, A. W., & Schiffman, P. (2003). Alteration of hyaloclastities in the HSDP 2 phase 1 drill core 1. Description and paragenesis. *Geochemistry Geophysics Geosystems*, *4*(5), 8709. https://doi.org/10.1029/2002GC000368

Wenk, H.-R., Joswig, W., Tagai, T., Korekawa, M., & Smith, B. K. (1980). The average structure of An 62-66 labradorite. *American Mineralogist*, *65*, 81–95.

Wenk, H.-R., & Van Houtte, P. (2004). Texture and anisotropy. *Reports on Progress in Physics*, *67*(8), 1367–1428. https://doi.org/10.1088/0034-4885/67/8/R02

Wohletz, K., Zimanowski, B., & Buttner, R. (2013). Magma-water interactions. In S. A. Fagents, T. K. P. Gregg, & R. M. C. Lopes (Eds.), *Modeling volcanic processes*, (pp. 230–256). Cambridge: Cambridge University Press. https://doi.org/10.1017/CBO9781139021562.011

Zhou, Z., Fyfe, W. S., Tazaki, K., & Van de Gaast, S. J. (1992). The structural characteristics of palagonite from DSDP site 335. *Canadian Mineralogist*, *30*, 75–81.